CFD SIMULATION OF VORTEX-INDUCED VIBRATION OF FREE-STANDING HYBRID RISER

A Thesis

by

YI CAO

Submitted to the Office of Graduate and Professional Studies of
Texas A&M University
in partial fulfillment of the requirements for the degree of

MASTER OF SCIENCE

Chair of Committee,	Hamn-Ching Chen
Committee Members,	Richard Mercier
	Prabir Daripa
Head of Department,	Sharath Girimaji

May 2017

Major Subject: Ocean Engineering

ABSTRACT

This thesis presents a 3D numerical simulation for a Free Standing Hybrid Riser under Vortex Induced Vibration, with prescribed motion on the top to replace the motion of the buoyancy can. The model is calculated using a fully implicit discretization scheme. The flow field around the riser is computed by solving the Navier-Stokes equations numerically. The fluid domain is discretized using the Chimera grid approach. Grid points in near-wall regions of riser are of high resolution, while far field flow is in relatively coarse grid. Fluid-structure interaction is accomplished by communication between fluid solver and riser motion solver.

Simulation is based on previous experimental data. Two cases are studied with different current speeds, where the motion of the buoyancy can is approximated to a 'banana' shape. A fully three-dimensional CFD approach for VIV simulation for a top side moving Riser has been presented.

DEDICATION

This thesis is dedicated to my wife Ada Guo. Her encouragement and understanding have been with me since the beginning of the research.

Also, this thesis is dedicated to my parents who supported me both mentally and financially.

ACKNOWLEDGEMENTS

I would like to thank my committee chair, Dr. Chen, and my committee members, Dr. Mercier and Dr. Daripa, for their guidance and support throughout the course of this research.

Thanks also go to my friends and classmates and the department faculty and staff for making my time at Texas A&M University a wonderful experience. I also want to thank the Texas A&M University Supercomputer Center, which provided the necessary facilities for my research work.

CONTRIBUTORS AND FUNDING SOURCES

This work was supervised by a thesis committee consisting of Professor Hamn-Ching Chen and Professor Richard Mercier of the Department of Civil Engineering and Professor Prabir Daripa of the Department of Mathematics.

All work for the thesis was completed independently by the student.

There are no outside funding contributions to acknowledge related to the research and compilation of this document.

NOMENCLATURE

2D	Two Dimensional
3D	Three Dimensional
Cd	Drag Coefficient
CFD	Computational Fluid Dynamics
Cl	Lift Coefficient
D	Riser Outer Diameter
D_s	Riser Damping
DNS	Direct Numerical Simulation
E	Young's Modules
EI	Bending Stiffness
FANS	Finite-Analytic Navier-Stokes
FFT	Fast Fourier Transform
FSHR	Free Standing Hybrid Riser
FSI	Fluid-Structure Interaction
GOM	Gulf of Mexico
I	Moment of Inertia
L	Riser Overall Length
LES	Large Eddy Simulation
M	Riser Unit Mass

MARIN	Maritime Research Institute Netherlands
N-S	Navier-Stokes
RANS	Reynold-Averaged Navier-Stokes
T	Tension
U	Velocity of Current
VIM	Vortex-Induced Motion
VIV	Vortex-Induced Vibration

TABLE OF CONTENTS

Page

LIST OF FIGURES

Page

LIST OF TABLES

Page

CHAPTER I

INTRODUCTION AND LITERATURE REVIEW

As oil and gas exploration and production activities are focusing more on deep waters, free standing and hybrid risers are finding its applications in these fields all over the world increasingly. The first FSHR was developed and deployed in the Campos Basin in Brazil in Oct. 2007. In Dec. 2009 and early 2010, the first five disconnectable FSHRs were successfully deployed for the Cascade and Chinook field development in the Gulf of Mexico. Since then, the FSHR concept has been widely recognized within the deep-water offshore industry and is likely to become one of the most attractive riser concepts.

Free Standing Hybrid Riser (FSHR) is capable of transferring fluids from seabed to a floating vessel and vice versa, with little influences of environmental loads and vessel motions (Pereira et al., 2005; Song et al., 2010). A typical system of FSHR is shown in Figure 1. FSHR consists of a vertical steel pipe tensioned by a submerged buoyancy can. The top of the riser is connected to a buoyancy can which links the production platform using a flexible jumper. The bottom of the riser is attached to a seabed foundation and a rigid jumper connects the FSHR to the pipeline end termination.

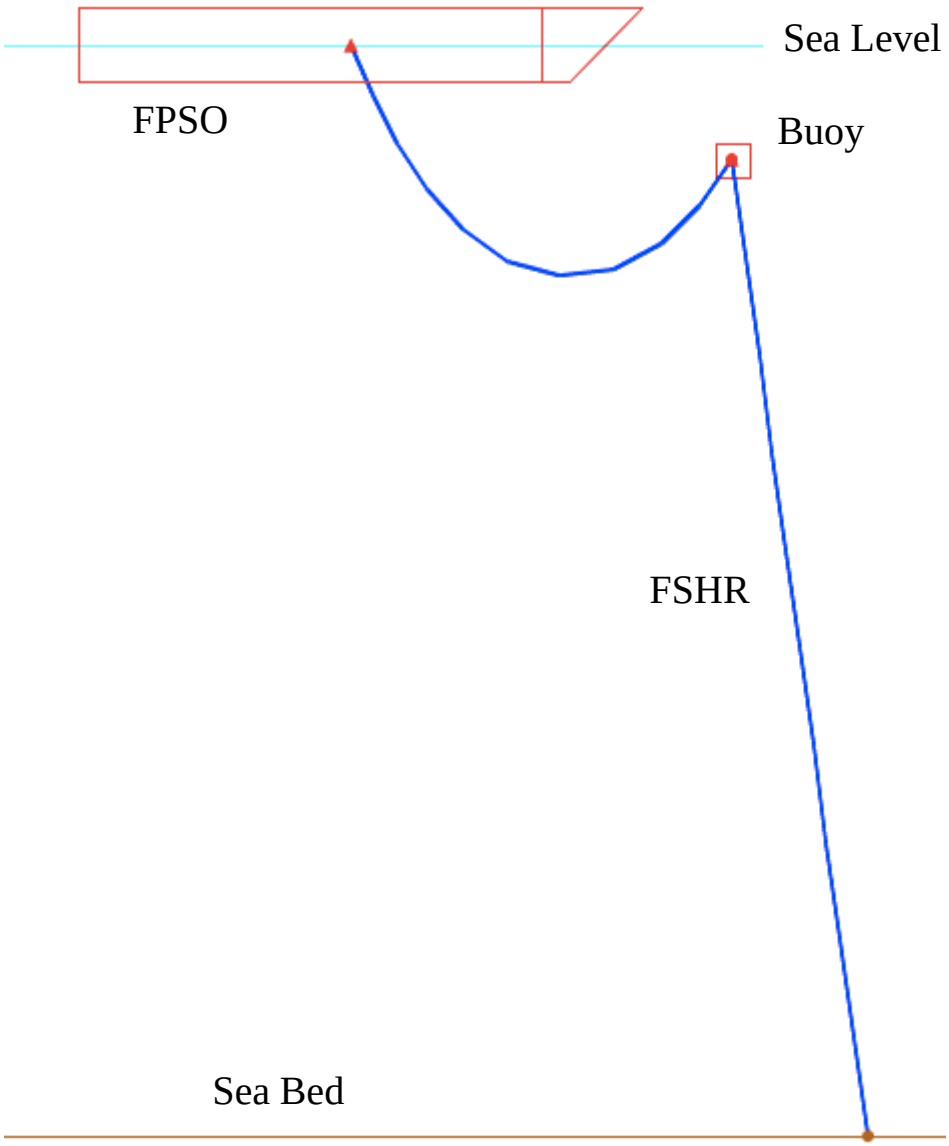

Figure 1 Free Standing Hybrid Riser System

There are many benefits of FSHR in deep water. First of all, FSHR can be installed before or after the floating production unit is anchored on site. This offers a

greater flexibility with respect to time during installation. Secondly, because the riser is tensioned by the air can, it can support its own weight. Therefore, the production platform doesn't need to carry the heavy payload, in deep water situations. Although there are various versions of the FSHR and the configuration has been modified so many times, the key technical benefit of this concept remains that the rigid vertical riser is decoupled from the floating production unit (FPU). The connection is achieved through a flexible jumper. Hence the riser is insensitive to the fatigue caused by the motion of the FPU. Since the fatigue design of the deep-water risers has always been a big challenge, the decoupling effect improves FSHR performance significantly. Numerous FSHR systems have been installed in West coast of Africa in the past few years. And recently in Brazil and Gulf of Mexico (GOM), plenty of deeper applications are being conducted.

The research of the vortex induced motion of FSHR has been conducted through experiments. In 2006, Wilde at MARIN (Maritime Research Institute Netherlands) conducted tow tank experiments to study the VIV response of a FSHR. The experiments were conducted in MARIN's Depressurised Towing Tank facility having dimension of 240 m in length, 18 m in width and 8 m in depth. The overhead carriage can maintain an accurate speed between 0 and 8 m/s. The free standing riser model was towed by the carriage using a 200 kg clump weight, hanging from the carriage on 4 steel wires at approximately 7 m water depth. The riser model was mounted at its bottom with a uni-joint on the clump weight. The FSHR model was tested in uniform current conditions with virtually no background turbulence. VIV responses of the riser and buoyancy at different uniform current conditions are observed.

Due to the development of computational techniques, numerical simulation has played an increasingly significant role in Offshore VIV problems recently, which is also considered as a valuable alternative to experiments. Rakshit et al. (2008), using CFD, simulated a long slender riser, made of composite materials and subject to an ocean current. They studied the influence of the number of modes as well as the influence of mass ratios and the value of the damping coefficient. They found that the vibration amplitude increases with the number of modes. Wang et al. (2010) published his research of VIV on 2D circular riser using a high resolution numerical scheme. The paper presents a high resolution numerical method for VIV simulation on the fluid structure interaction (FSI) of circular cylinder which represents a two dimensional marine riser. The comparison of their FSI prediction and the available experimental data showed a good agreement in a wide range of Reynolds number. Huang et al. (2007) released their research about vertical riser VIV simulation in uniform current. They compared their simulation results with the experimental data donated by ExxonMobil URC, Houston, TX, USA. It is concluded that the present CFD method is capable of providing reasonable results and is suitable for 3D riser VIV analysis in deep water and complex current conditions.

In recent years, numerical methods took part in the analysis of FSHR. Cheng et al. (2006, 2007) presented time domain riser VIV research using ABAVIV code. Based on these studies, Liu et al. (2009) presented a research of time domain VIV analysis of a FSHR. The analysis was performed using a time domain VIV code ABAVIV, which uses ABAQUS to calculate the response from the VIV forcing. This is the first

application of this method to a FSHR. Their models and analysis tools are now accepted by Technip for VIV and VIM behavior of FSHR system analysis.

Although riser VIV CFD simulation is quite popular these days, researches about FSHR VIV have not been fully studied. A 3D numerical simulation for a free standing hybrid riser under interactions is presented in this thesis. We use a prescribed motion on the top of the riser to replace the oscillation of the buoyancy can. Finite element method was applied to the model using a fully implicit discretization scheme (Huang., et al 2011). The flow field around riser is computed by solving the incompressible Navier-Stokes equations numerically. Chimera grid approach is adopted to generate the fluid domain. Fluid-structure interaction is accomplished by communication between fluid solver and riser motion solver. The motion solver inputs drag and lift forces calculated by fluid solver and calculate the displacements in in-line and cross-line directions. Then motion solver outputs new positions of pipeline back to fluid solver.

Simulation is based on the experimental data from Wilde's model tests. Riser particulars used in the simulation are the same as the parameters provided by the experiment. Two cases with different current speed were simulated and analyzed.

CHAPTER II

NUMERICAL APPROACH FOR RISER VIV SIMULATION

This Chapter demonstrates the numerical approach for the riser VIV simulations, including computational fluid dynamics method, riser motion solver development and fluid-structure interactions.

The numerical approach we adopted is a Finite-Analytic Navier-Stokes (FANS) code. This time domain simulation code can calculate the flow field around the riser by solving the unsteady, incompressible Navier-Stokes equations numerically. The turbulent flow was solved using Large Eddy Simulation (LES) model. The code has been previously validated through multiple applications (Chen et al., 1988, 1989, 1990, 2013; Pontaza et al., 2005, 2006; Huang et al., 2007, 2008, 2011, 2012).

Incompressible Navier-Stokes Equations

Navier-Stokes equations, named after Claude-Louis Navier and George Gabriel Stokes, describe the motion of viscous fluid substances. The equations combine Newton's second law with fluid motion with the assumption that the stress in the fluid is the sum of a diffusing viscous term (proportional to the gradient of velocity) and a pressure term.

Unlike normal classical mechanics, where solutions are typically position of a particle or deflection of a continuum, the solution of the N-S equations is a flow velocity. Once the velocity field is calculated, other quantities, such as pressure or temperature, can be found.

We write the stationary Navier-Stokes equations in dimensionless form as follows (Pontaza et al., 2005; Rehman et al., 2007):

$$(u \cdot \nabla)u + \nabla p - \frac{1}{R_e}\nabla \cdot \left[(\nabla u) + (\nabla u)^T \right] = f \text{ in } \Omega \tag{1}$$

$$\nabla \cdot u = 0 \text{ in } \Omega, \tag{2}$$

Equation (1) represents the momentum equation. Where $u(x)$ represents velocity, $p(x)$ is pressure, R_e is the Reynolds number and f is a dimensionless force.

Incompressible flow refers to a flow whose density is constant within a fluid parcel. An equivalent statement for incompressibility is that the divergence of the flow velocity is zero. Equation (2) is the continuity equation or mass conservation equation for incompressible flow.

The derivation of $\nabla \cdot u = 0$ is based on $\frac{d\rho}{dt} = 0$

$$\frac{d\rho}{dt} = \frac{\partial \rho}{\partial t} + \frac{\partial \rho}{\partial x}\frac{dx}{dt} + \frac{\partial \rho}{\partial y}\frac{dy}{dt} + \frac{\partial \rho}{\partial z}\frac{dz}{dt} = \frac{\partial \rho}{\partial t} + \nabla \rho \cdot u = 0 \tag{3}$$

The conservation of mass equation can be written as:

$$\frac{\partial \rho}{\partial t} + \nabla \cdot (\rho u) = \frac{\partial \rho}{\partial t} + \nabla \rho \cdot u + \rho(\nabla \cdot u) = 0 \tag{4}$$

Combining two equations above, we can get:

$$\frac{d\rho}{dt} = -\rho(\nabla \cdot u) = 0 \tag{5}$$

The code used in this research is called Chimera Finite-Analytic Reynolds-Averaged Navier-Stokes Program, developed by Chen (1988). The code transforms the governing equations from physical coordinates (x, y, z) in to numerical coordinates (ζ, η, γ). A finite-volume scheme was adopted to solve the continuity equation. The convective transport equations for mean velocities and turbulence parameters are solved by the finite-analytic method in the transformed domain (Chen et al., 1990). The pressure field is then updated by a SIMPLER algorithm (Chen et al, 1988, 1989).

Overset Grid

Overset grid, also called Chimera grid, is used for dynamically simulating riser motion in a uniform current. A common difficulty in complex CFD simulation is that not every geometry can be well represented using a single, contiguous grid. In many cases, different geometrical characteristics can be best described by different types of grids. These subdomains are also referred to as blocks, which have overlapping areas at the interface between every two neighboring blocks. Boundary information is exchanged between these blocks via interpolation at the fringe points, which lie in the interior of the neighboring blocks. Some grid-points may not be used in the solution, which are called hole points. In general terms, there are three steps to set up an overset grid:

1. Grid generation;
2. Hole cutting;
3. Interpolation

A typical overset grid is shown in Figure 2. The red grid around the surface of the riser is in polar coordinate and the green grid is in Cartesian coordinate. The coordinate system is selected as: x direction coincides with riser axis, y is the current direction, and z is the cross flow direction. Usually, structured-curvilinear grids combined with Cartesian grid are often used for complex geometries. When several geometric components occur in one fluid domain, their high quality body-fitting curvilinear grid can be generated independently, and then embedded into the same Cartesian background grid.

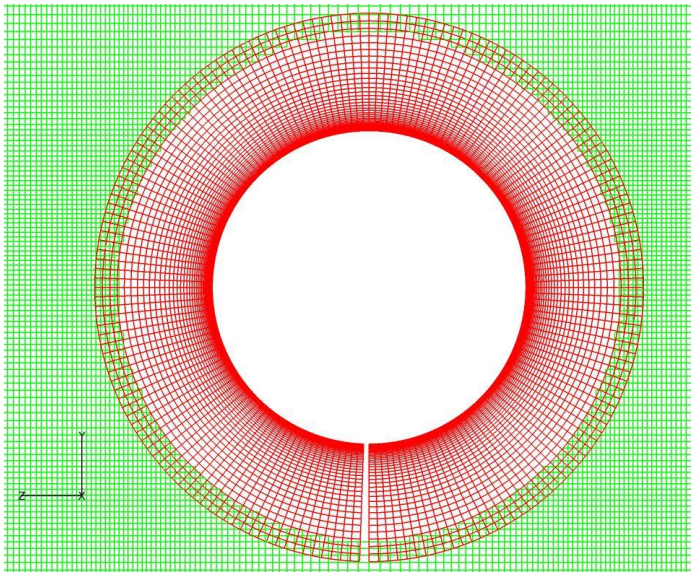

Figure 2 Overset Grid

In some systems, any of the three steps which generate the overset grid can be combined as one step. In this research, we use PEGSUS 4.0 (Suhs et al., 1991) to conduct part of the grid generation. The code is able to cut the hole as well as conduct the interpolation. The elimination of the grids is accomplished by setting a hole creation boundary within the red grid. Inside that boundary, all green grids are to be deleted. The points in the green grid surrounding the deleted points are boundary points, and they receive flow field information interpolated from grid points within the red block. Vice versa, the points on the outer boundary of the red block also receive flow field information from the grid points in the green block.

Using overset grid allows us to manipulate the resolution of the particular portion of the grid without changing the other parts. In this case, the computational grid is modified to very fine resolution near the riser outer boundary, whereas the far field grid

is relatively coarse. This adjustment reduces the total element number and thus saves a lot of calculation time.

In this research, we use two computational blocks to simulate the whole fluid domain: near body grid and wake grid. A typical cross section of this approach is shown in Figure 3. The near body grid (red) is generated in polar coordinate. Wall boundary condition is applied surround the surface of the riser. Wake grid (green) is generated in Cartesian coordinate right surrounding the near body grid. The grid has very good concentration around the near body grid, while at far flied area, the grid is relatively coarse. This grid distribution provide fine enough calculation domain for vortex shedding and can save more computation effort than the uniform grid. At the interface between near grid and wake grid, we try to make the sizes of the grid from each block of the same magnitude in order to guarantee the accuracy of the communication of the flow field information.

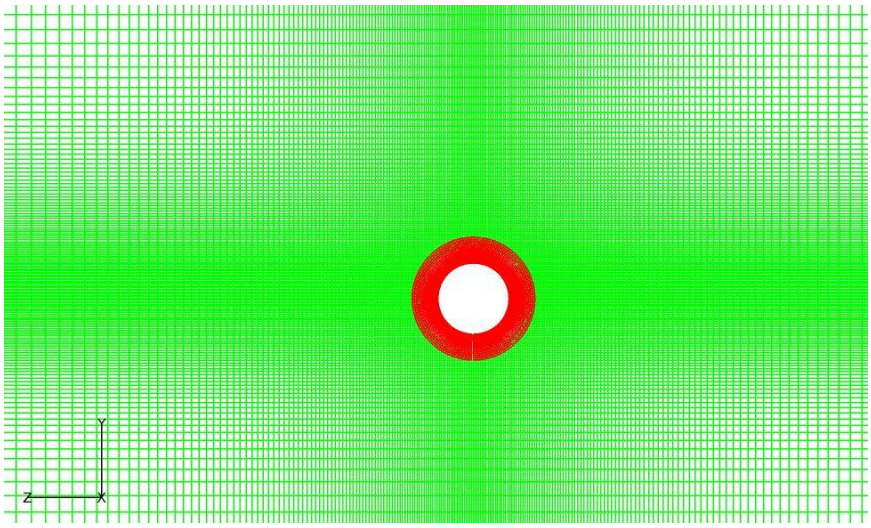

Figure 3 2D Cross Section Grid for VIV Simulation

The two-dimensional meshing scheme mentioned above is accomplished by a re-spline program (Korpus et al., 1990). The code is developed to re-spline a three-dimensional grid. The re-splining is performed independently in each direction. By running the re-spline program twice, we can get the cross section we need. As for the riser axial direction, we divide the flow field into many parallel layers. Because the current is propagating perpendicular to the axial direction in the in-line direction, there is no velocity change in the x direction. Thus, we use coarse grid in the span-wise direction and there is no need to re-spline it.

A dynamic grid scheme (a moving grid) is also employed in this approach. As the riser moves, the near body grid and wake grid will move with the riser at the same velocity. This synchronous movement guarantees that there is no gap between the riser boundary and fluid boundary. Through moving grid, we eliminate the need to generate a grid at each time step, which is a time consuming process of CFD calculation. We only need to move the existing blocks and determine the new interaction between two blocks.

Motion Solver

A riser can be modeled as a tensioned beam in the in-line and cross-flow directions separately. The tension distribution varies linearly in the axial direction. In the reality, the top tensioned risers have the highest tension at the top, and lowest tension at the bottom due to its own submerged weight. The governing equations of a tensioned beam are described as:

$$T\frac{d^2y}{dx^2}+\frac{dy}{dx}\frac{dT}{dx}-\frac{d^2}{dx^2}\left(EI\frac{d^2y}{dx^2}\right)+F_y=M\ddot{y}+D_S\dot{y} \tag{6}$$

$$T\frac{d^2z}{dx^2}+\frac{dz}{dx}\frac{dT}{dx}-\frac{d^2}{dx^2}\left(EI\frac{d^2z}{dx^2}\right)+F_z=M\ddot{z}+D_S\dot{z} \tag{7}$$

Where T is the axial tension, F_y and F_z are the external forces in y and z directions, x is the axial direction, y is the in-line direction, z is the cross-flow direction, E is Young's modulus, I is the area moment of inertia, D_s is the damping ratio and M is the mass of riser in unit length. A finite difference scheme (Huang, 2011; Xiao, 2015) was adopted to discretize the governing equation in the in-line directions (discretization in the z direction is in the same pattern):

$$\frac{dy}{dx}=\frac{y_{j+1}^n-y_{j-1}^n}{2\Delta x}\text{, For j=2…N-1,} \tag{8}$$

$$\frac{dy}{dx}=\frac{-3y_j^n+4y_{j+1}^n-y_{j+2}^n}{2\Delta x}\text{, For j=1,} \tag{9}$$

$$\frac{dy}{dx}=\frac{y_{j-2}^n-4y_{j-1}^n+3y_j^n}{2\Delta x}\text{, For j=N,} \tag{10}$$

$$\frac{d^2y}{dx^2} = \frac{y_{j-1}^n - 2y_j^n + y_{j+1}^n}{\Delta x^2}, \text{ For j=2…N-1,} \tag{11}$$

$$\frac{d^2y}{dx^2} = \frac{y_j^n - 2y_{j+1}^n + y_{j+2}^n}{\Delta x^2}, \text{ For j=1,} \tag{12}$$

$$\frac{d^2y}{dx^2} = \frac{y_{j-2}^n - 2y_{j-1}^n + y_j^n}{\Delta x^2}, \text{ For j=N,} \tag{13}$$

$$\frac{d^4y}{dx^4} = \frac{y_{j-2}^n - 4y_{j-1}^n + 6y_j^n - 4y_{j+1}^n + y_{j+2}^n}{\Delta x^4}, \text{ For j=3…N-2,} \tag{14}$$

$$\frac{d^4y}{dx^4} = \frac{y_j^n - 4y_{j+1}^n + 6y_{j+2}^n - 4y_{j+3}^n + y_{j+4}^n}{\Delta x^4}, \text{ For j=1,} \tag{15}$$

$$\frac{d^4y}{dx^4} = \frac{y_{j-1}^n - 4y_j^n + 6y_{j+1}^n - 4y_{j+2}^n + y_{j+3}^n}{\Delta x^4}, \text{ For j=2,} \tag{16}$$

$$\frac{d^4y}{dx^4} = \frac{y_{j-3}^n - 4y_{j-2}^n + 6y_{j-1}^n - 4y_j^n + y_{j+1}^n}{\Delta x^4}, \text{ For j=N-1,} \tag{17}$$

$$\frac{d^4y}{dx^4} = \frac{y_{j-4}^n - 4y_{j-3}^n + 6y_{j-2}^n - 4y_{j-1}^n + y_j^n}{\Delta x^4}, \text{ For j=N,} \tag{18}$$

$$\ddot{y} = \frac{y_j^n - 2y_j^{n-1} + y_j^{n-2}}{\Delta t^2}, \text{ For n } \geq 3, \tag{19}$$

$$\dot{y} = \frac{y_j^n - y_j^{n-1}}{\Delta t}, \text{ For n } \geq 2. \tag{20}$$

After substituting equation (8) – (20) into equation (6) and (7), we get the discretization results are presented as:

$$\frac{EI}{\Delta x^4} y_{j-2}^n - (\frac{T_j}{\Delta x^2} - \frac{1}{2\Delta x}\frac{dT_j}{dx} + \frac{4EI}{\Delta x^4}) y_{j-1}^n + (\frac{2T_j}{\Delta x^2} + \frac{6EI}{\Delta x^4} + \frac{M}{\Delta t^2} + \frac{D_s}{\Delta t}) y_j^n$$

$$-(\frac{T_j}{\Delta x^2} - \frac{1}{2\Delta x}\frac{dT_j}{dx} + \frac{4EI}{\Delta x^4}) y_{j+1}^n + \frac{EI}{\Delta x^4} y_{j+2}^n$$

$$= F_{yj}^n + (\frac{2M}{\Delta t^2} + \frac{D_s}{\Delta t}) y_j^{n-1} - \frac{M}{\Delta t^2} y_j^{n-2} \tag{21}$$

$$\frac{EI}{\Delta x^4} z_{j-2}^n - (\frac{T_j}{\Delta x^2} - \frac{1}{2\Delta x}\frac{dT_j}{dx} + \frac{4EI}{\Delta x^4}) z_{j-1}^n + (\frac{2T_j}{\Delta x^2} + \frac{6EI}{\Delta x^4} + \frac{M}{\Delta t^2} + \frac{D_s}{\Delta t}) z_j^n$$

$$-(\frac{T_j}{\Delta x^2} - \frac{1}{2\Delta x}\frac{dT_j}{dx} + \frac{4EI}{\Delta x^4}) z_{j+1}^n + \frac{EI}{\Delta x^4} z_{j+2}^n$$

$$= F_{zj}^n + (\frac{2M}{\Delta t^2} + \frac{D_s}{\Delta t}) y_j^{n-1} - \frac{M}{\Delta t^2} z_j^{n-2} \tag{22}$$

Δt is the time step, and n denotes the time step. Δx is the length of a riser's segment. In this research, we discretize the riser into 250 segments. The discretization is applied for both in-line and cross-flow direction. Parameters *T*, *EI*, *M*, D_s are declared through the riser input file. External forces F_y and F_z are obtained from the fluid solver. And the riser displacements at each node are computed by the motion solver.

We solve equation (21) and (22) in matrix forms:

$$[A][Y] = [F] \tag{23}$$

Where A is an N×N matrix, representing the stiffness of the tensioned beam, extracted from the left sides of equation (21) & (22). Matrix Y = $\begin{pmatrix} y_1 \\ y_2 \\ \vdots \\ y_N \end{pmatrix}$ represents the displacement at each node. Matrix F represents the force terms on the right sides of the equations. By solving that matrix equation (23), we can calculate the displacement at each time step.

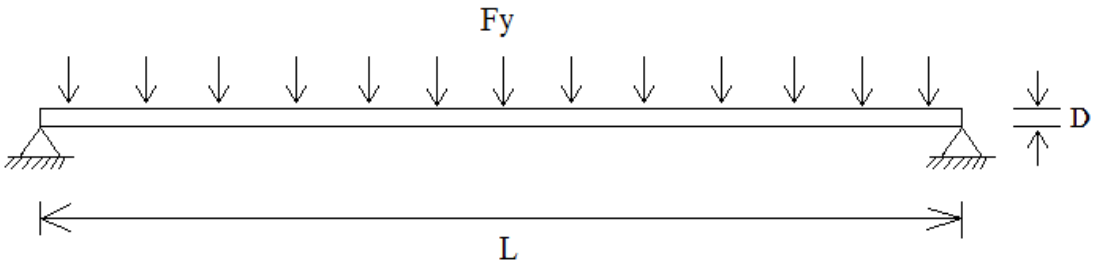

Figure 4 Static Validation Case for Pipeline Motion Solver

In order to verify the accuracy of this riser motion solver, we check two cases against the theoretical solution: (1) a riser with constant tension, (2) a riser with linearly distributed tension. In the reality, the riser is standing vertically, with the tension on the top provided by the buoyancy can and the tension at the bottom provided by the base structure. Due to its own submerged weight, the tension is highest on the top and lowest at the bottom. The results are shown in the Figure 5 and Figure 6. For constant tension

case, the riser displacement is symmetric and the maximum deflection occurs in the middle of the riser. As for the varying tension case, the displacement is not symmetric and the maximum riser deflection occurs somewhere in the lower portion of the riser. For both cases, our motion solver's solution exactly follows the theoretical solution.

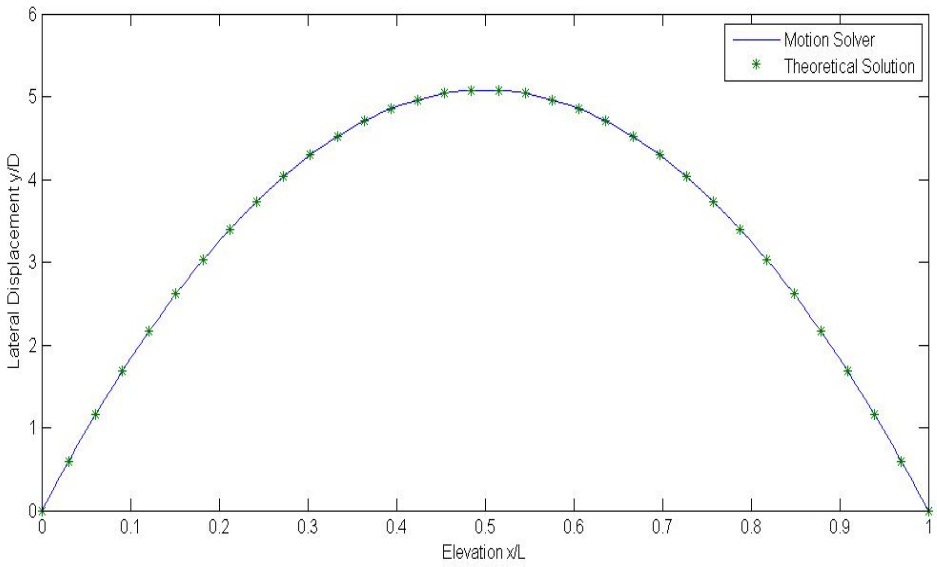

Figure 5 Riser Static Displacement Comparison (Constant Tension)

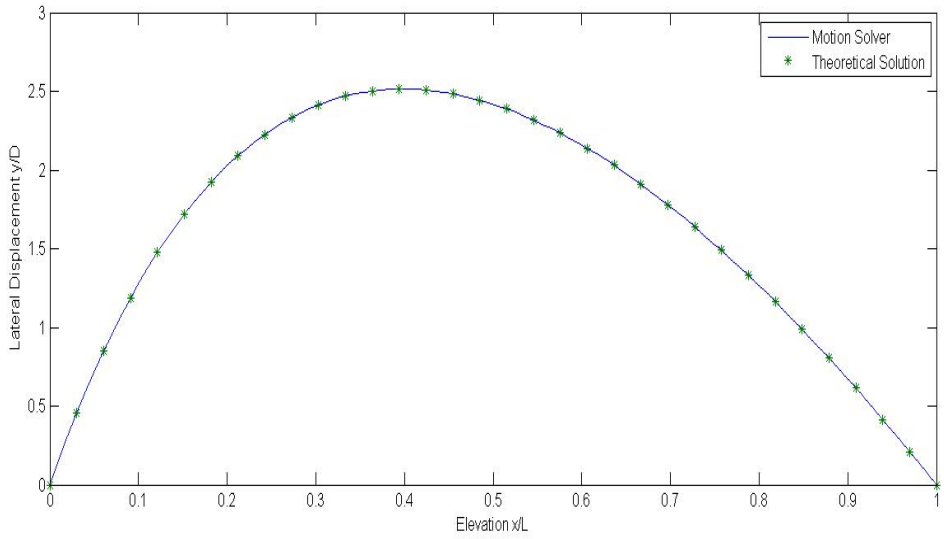

Figure 6 Riser Static Displacement Comparison (Varying Tension)

Another case to verify the motion solver is set in dynamical conditions. Figure 7 demonstrates the case. A riser with constant tension has one end pinged to the wall and the other end moving in a prescribed motion.

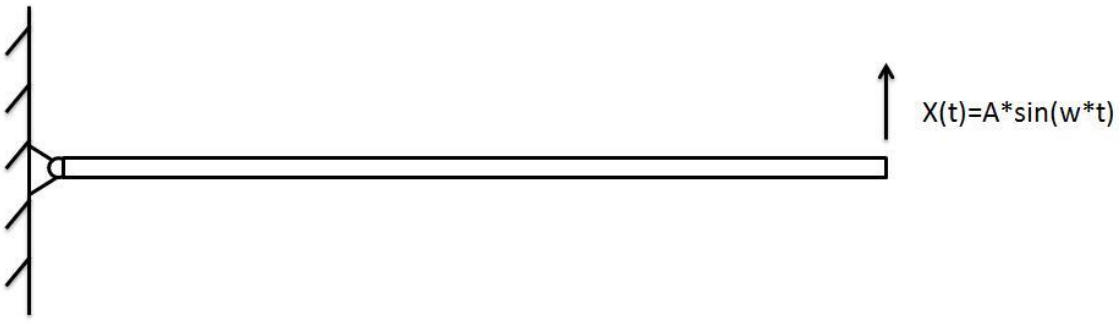

Figure 7 Dynamic Validation Case for Riser Motion Solver

The prescribed motion we impose at the free end of the riser is following *X(t)=A*sin(wt). A* is the amplitude of the motion, and *w* implies the frequency of the movement. We use commercial software OrcaFlex, a package for dynamic analysis of offshore marine systems, to do the comparison.

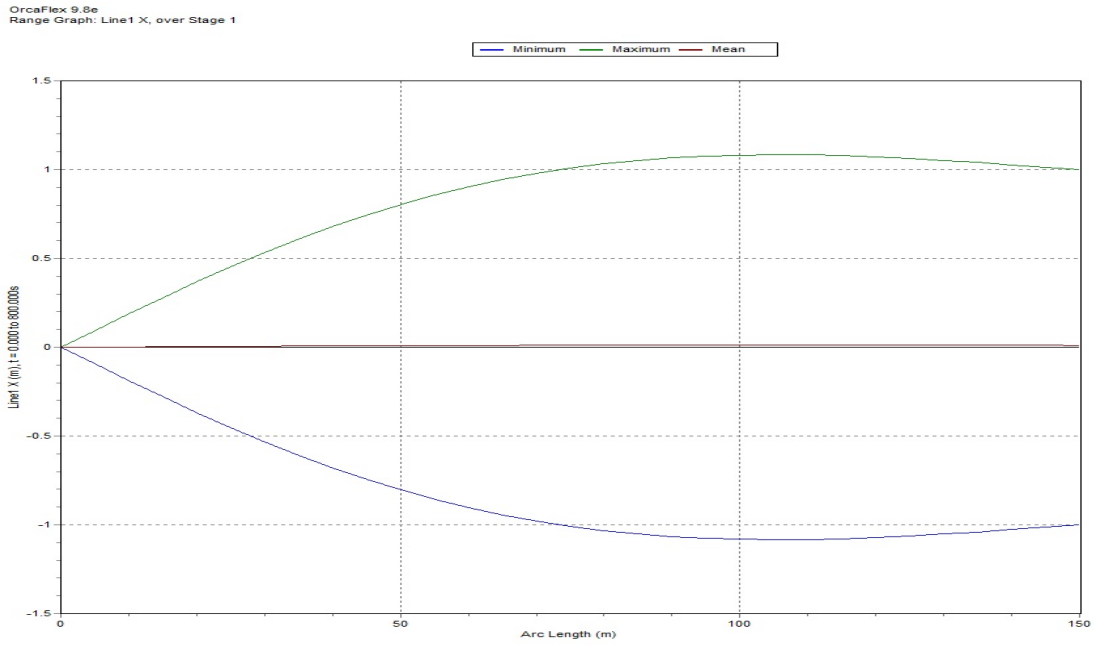

Figure 8 Riser Envelop by OrcaFlex

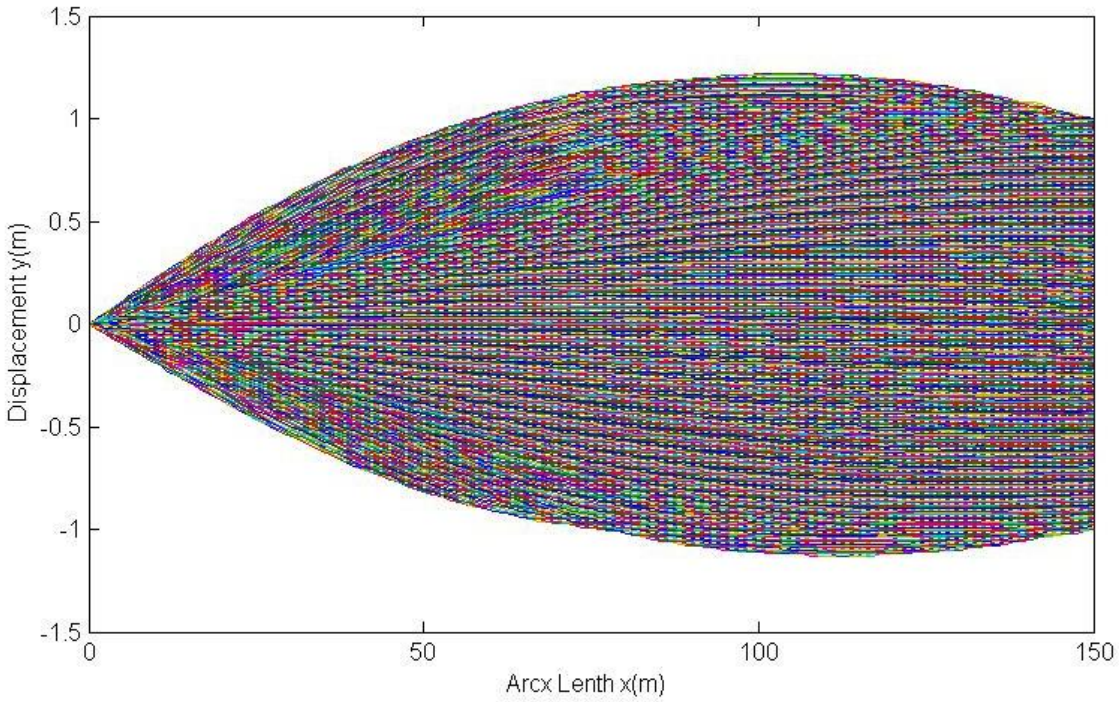

Figure 9 Riser Envelop by Motion Solver

At a specific tension, length, Young's modulus and movement frequency, the vibration envelop has the shape shown in Figure 8, which is generated by OrcaFlex. The result computed by our motion solver is shown in Figure 9. The two comparisons agree with each other.

CFD Simulation Procedures

Fluid-structure interaction problems and multi-physics problems are usually too complex to solve analytically. These problems are dealt with using experiments or numerical simulation. The maturity of computational fluid dynamics has enabled numerical simulation of fluid-structure interaction. There are two main approaches that exist for the FSI problems: Monolithic approach and Partitioned approach.

The method we adopted in this research is partitioned approach: the equation governing the flow and the displacement of the riser are solved separately in two distinct solvers (Bungartz et al,. 2006). The procedure of FSI is demonstrated in Figure 10. At each time step, the fluid solver, based on the displacement information of the riser, solves the Navier-Stokes equation numerically and obtain the pressure and force of the whole flow field. Drag and lift forces are then read by riser motion solver as input to calculate the new position for next step computation. In this way, the FSI problem is solved in a partitioned approach.

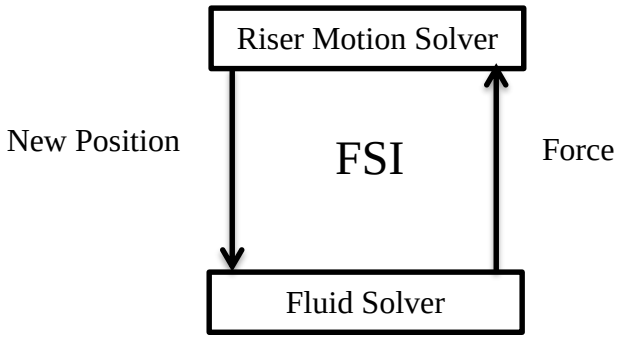

Figure 10 Fluid-Structure Interaction Procedure

The total computational fluid dynamics simulation procedures are shown in the Figure 11. At the beginning, we generate the overset grid we need using the methods mentioned above. Then with the initial riser position and flow field setting, the fluid solver starts to compute velocity and pressure. The motion solver then read in the Drag coefficient (Cd) and Lift coefficient (Cl) to calculate the new riser position. Next, the grids move according to the riser displacement generating new grid interpolation coefficients. The fluid solver then uses this information and begins calculation for the next step.

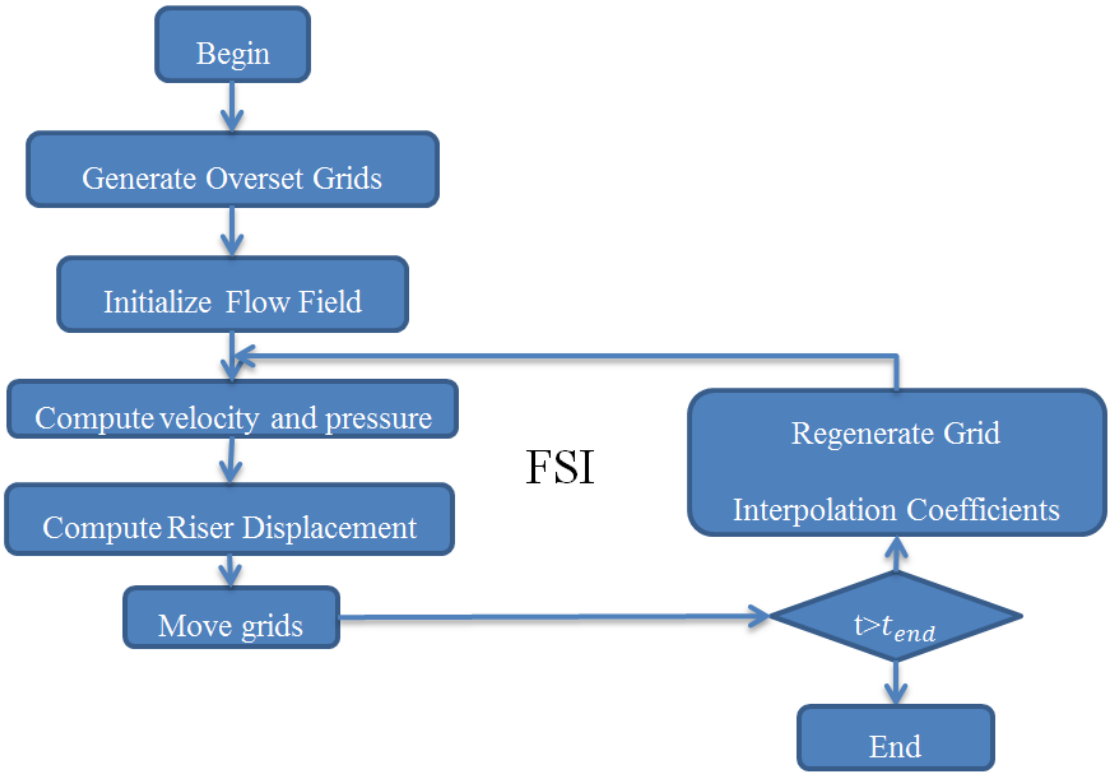

Figure 11 CFD Simulation Procedures

CHAPTER III

VIV SIMULATION OF A FSHR

During the last decades, many VIV experiments have being performed and published on deep water slender bodies. However, the research especially focused on the Free Standing Hybrid Riser is relatively rare. Wilde (2007) did model tests on the VIV of the air can of a Free Standing Riser System in current. The experiment was carried out at MARIN (Maritime Research Institute Netherlands), in the depressurised towing tank. In our research, we are going to use Wilde's experimental results to benchmark our computer codes.

Experiment Background

The experiments were carried out in a towing tank, being 240 m long, 18 m wide and 8 m deep. As shown in Figure 12, the tank has an overhead carriage which can control accurate speed between 0 and 8 m/s. the riser model was mounted at its bottom connected to the clump through the uni-joint. The riser was also tensioned by the air can at the top. As the carriage moves at certain speed, the whole system moves together, including the riser. This simulate the situation that riser is under uniform current.

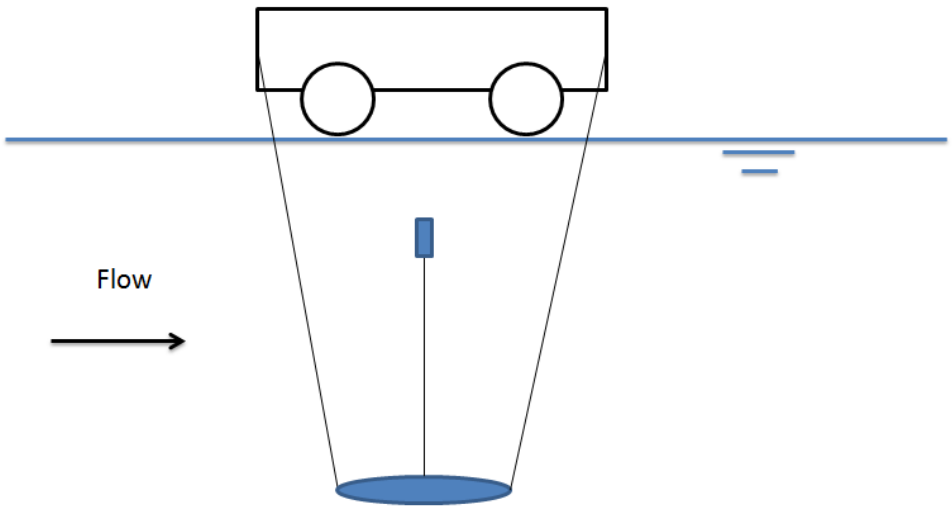

Figure 12 Test Setup

The riser model diameter is 0.008 m and the length over diameter is L/D = 625, which indicates a very long riser. The other parameters are provided in the following Tables. Table 1 provides information for the buoyancy can and Table 2 provides particulars for the vertical riser. A geometrical model scale of 1:68.75 was assumed. Froude scaling was used for the velocities, accelerations and loads.

Table 1 Parameters of air can

Parameter	Symbol	Model Scale	Full Scale
Diameter	OD	80 mm	5.5 m
Length	L	495 mm	34.0 m
Weight in air	m	867 gr	2,833 KN
Mass ratio	m+	0.35	0.35
Upward thrust	T	1,621 gr	5,167 KN

Table 2 Parameters of vertical riser

Parameter	Symbol	Model Scale	Full Scale
Diameter	OD	8 mm	550 mm
Wall thickness	T	1 mm	69 mm
Length	L	5 m	344 m
Young's modulus	E	3,000 N/mm^2	2.1E11 N/m^2
Bending stiffness	EI	0.412 Nm^2	3.25E8 Nm^2
Weight in air	m	64 gr/m	439 kg/m
Underwater weight	W	0.41 N/m	1,922 N/m
Tension on the top	T_{up}	5,167 KN	4505.832 KN

In this thesis, the buoyancy can movement was replaced by the prescribed motion on the top of the riser. The trajectory of the air can is shown in Figure 13 and Figure 14. As we can see, the motions of the air can at current speed 0.5 m/s and 0.83 m/s (full scale) are in 'banana' shape. At current speed 0.5 m/s, the cross flow VIV response of the buoyancy can is slightly less than the diameter of the air can (A/D ~ 0.9). The in line VIV response is about 0.15 riser diameters.

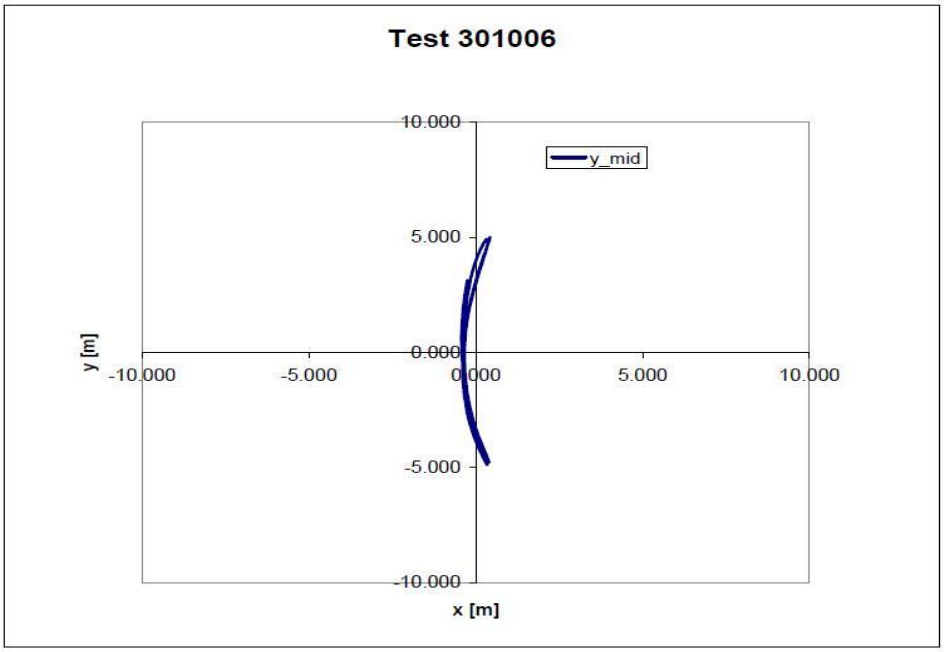

Figure 13 Buoyancy Can Trajectory at 0.50 m/s Current

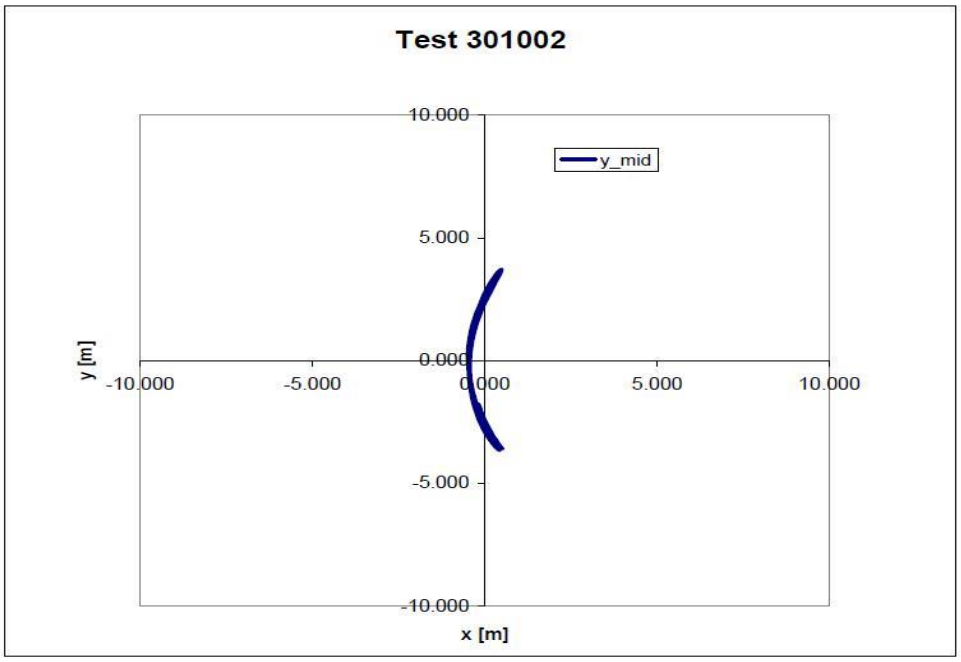

Figure 14 Buoyancy Can Trajectory at 0.83 m/s Current

In our computational grid, y is the in line direction, z is the cross flow direction. So we fit the displacement pattern as follows:

$$z(t) = A_Z \sin(wt) \tag{24}$$

$$y(t) = A_Y \sin(2wt + \theta) \tag{25}$$

A_Z is the average cross-stream amplitude of vibration. A_Z is the average in-line amplitude of vibration. $\omega = 2\pi f_Y$, with $\frac{f_Y}{f_Z} = 2$, θ is the phase angle. For different phase angles the trajectory will present different "figure of eight" shapes. For example, Figure 15, Figure 16, Figure 17 and Figure 18 show the shapes when θ equals π/6, π/3, π/2 and π.

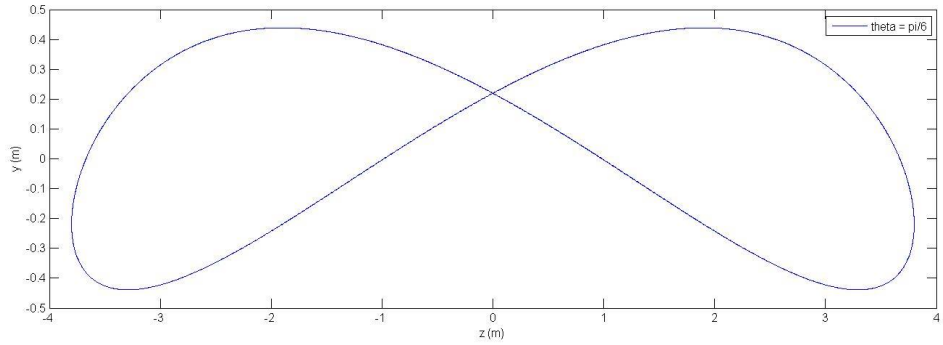

Figure 15 Trajectory for Theta = pi/6

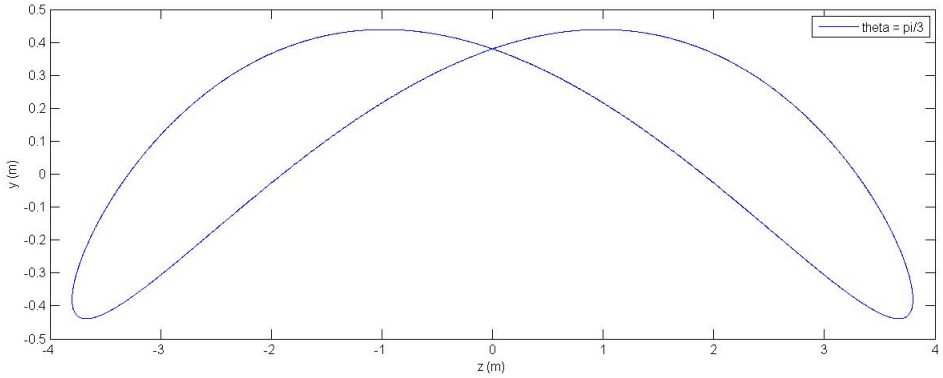

Figure 16 Trajectory for Theta = pi/3

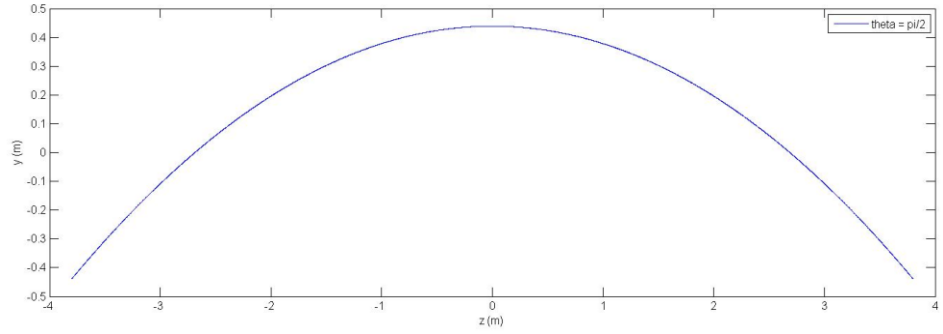

Figure 17 Trajectory for Theta = pi/2

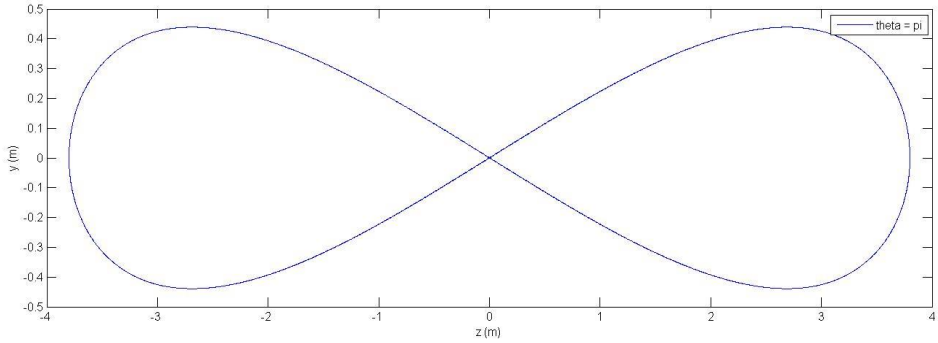

Figure 18 Trajectory for Theta = pi

The frequencies obtained from the experiment are 0.0132 Hz for current speed 0.5 m/s and 0.0191 Hz for current speed 0.83 m/s. Phase angle $\theta = \pi / 2$ for the final fit we adopted.

Grid Generation

The beginning stage of every CFD simulation is the generation of computational grid. As discussed before, an overset grid scheme is adopted in our research. For an isolated riser in infinite fluid domain, we use two blocks of grid: near body grid and wake grid. Figure 19 shows the wake grid with the near body grid implanted inside. Red block consists of 373100 (50*182*41) grid points and green block consists of 1593050 (50*151*211) grid points. There are about 2 million computational nodes in this simulation. The axial direction is divided into 50 layers and the length over diameter is 625.

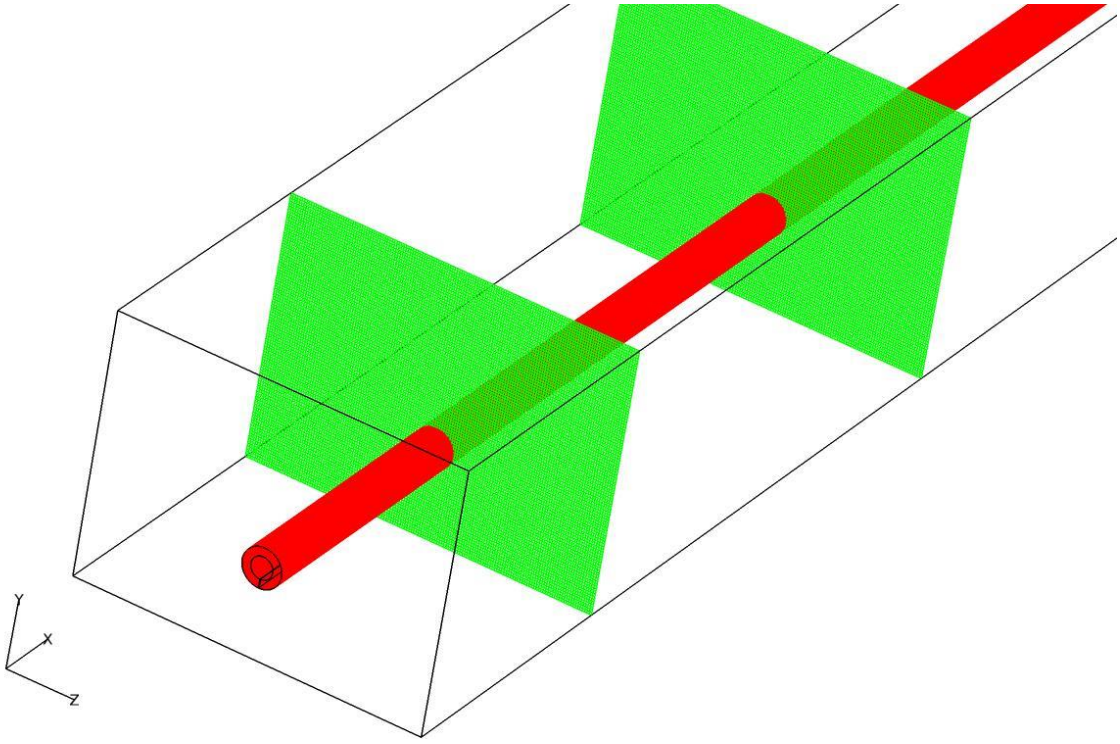

Figure 19 Overview of Fluid Domain for an Isolated Riser

The two-dimensional view of the cross section is presented in Figure 20. The riser is placed in the middle of the fluid domain. The riser center was set at the origin point (y, z) = (0, 0). The flow inlet (bottom side) is 8 D in front of the riser, while the flow outlet is 16 D behind the riser. Since we have prescribed “banana shape” motion, we make the lateral sides 16 D apart from the riser. The uniform current propagates in the positive Y direction (in-line direction).

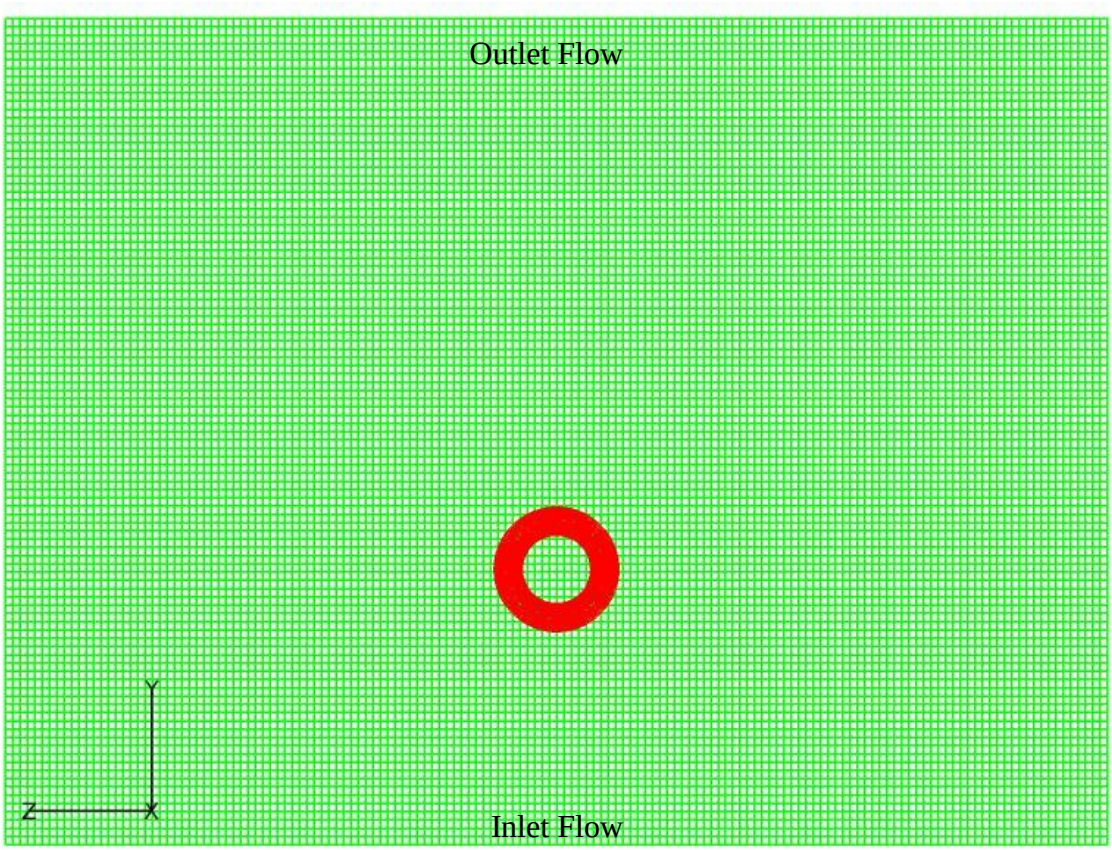

Figure 20 Cross Section of Fluid Domain

The red area is the near body grid, rather than the riser cross section. Figure 21 provides a close up view of the red grid. The inner boundary of the red grid is the riser outer boundary. And the red loop grid represents flow field around the riser. The near body grid consists of 50*182*41 grid points, with 49 elements in axial direction, 180 elements in circumferential direction and 40 elements in radial direction. In circumferential direction, 182 grid points create only 180 elements because node #182 overlap with node #2, while node #181 overlap with node #1. This overlapping allows flow information communication between these grid nodes.

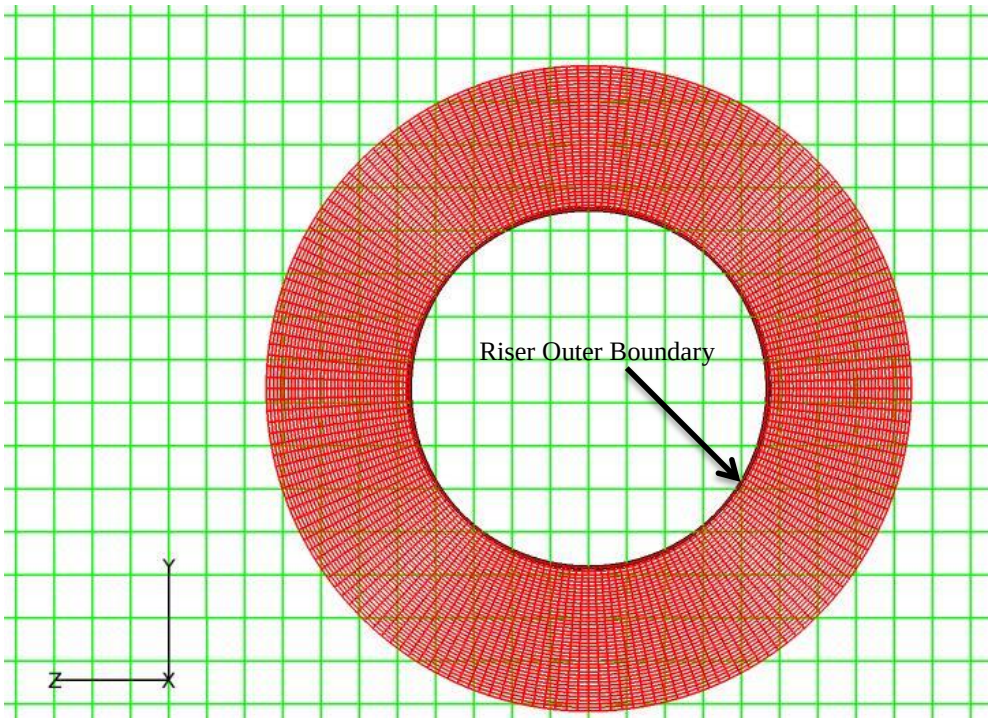

Figure 21 Near Body Grid

The grid generated above is uniformly distributed. It works well when the simulation domain is small. However, when you are specifying a large domain, there will be too many grid points inside the domain, which will cost tremendous calculation time. To solve this problem, we need to re-spline the grid. As we can imagine, the area surrounding the riser will have flow changing dramatically. For this area, a finer grid is needed. As for the far way field, the grid can be relatively coarse. The re-splined grid is presented in Figure 22 and Figure 23. In near wall block, the size of the innermost element is 0.001 D, while the outmost one is of 0.035 D. In the wake block, the finer grid is situated at the riser center and vice versa. The size of wake grid elements ranges from 0.025 D to 0.8 D in y direction and 0.025 to 0.3 D in z direction.

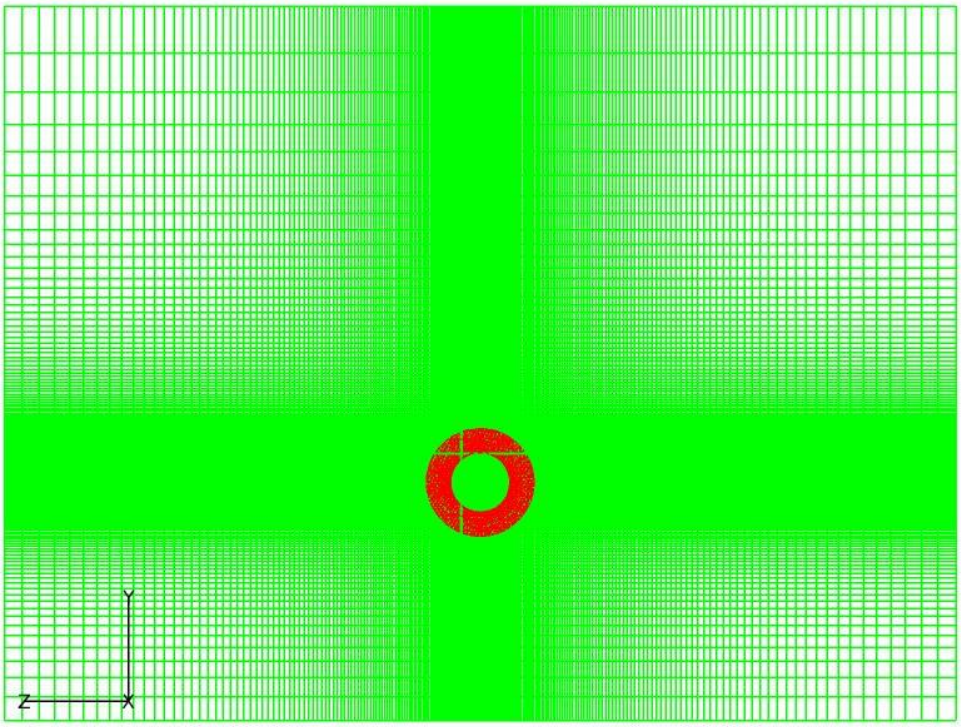

Figure 22 Overview of the Re-splined Grid

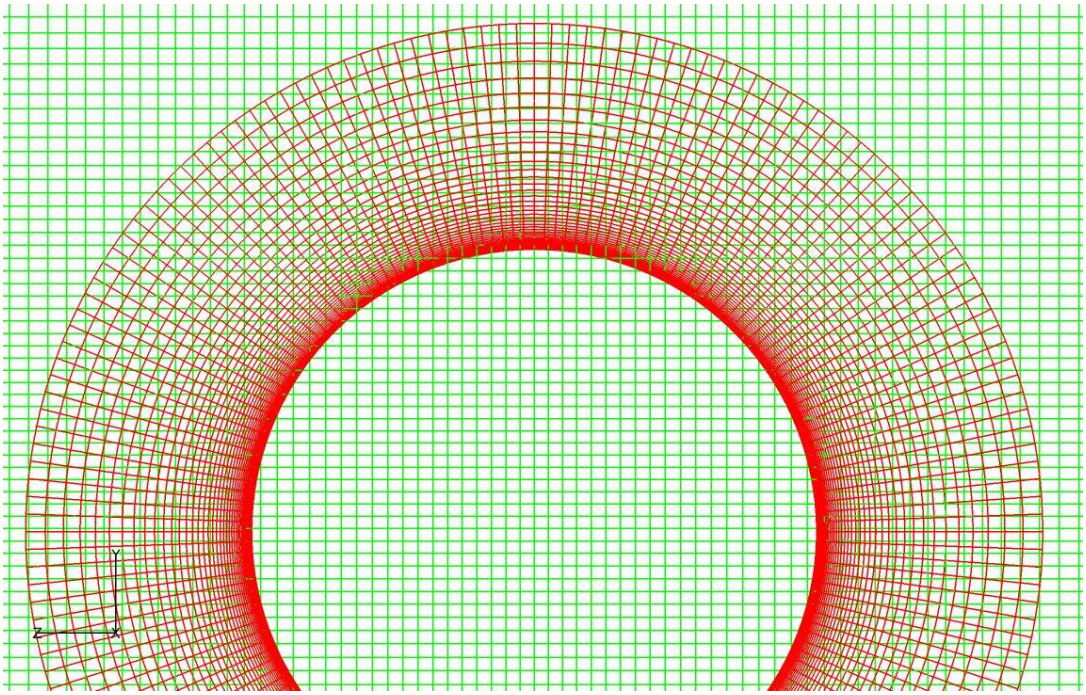

Figure 23 Near View of The Re-splined Grid

Whether the near body grid size at the outer boundary and the nearby wake grid size are close to each other, is essential to the interpolation between two grid sets. In Figure 24, red and green elements are about the same size. Red node 1 inside the green element ABCD, can receive flow information by interpolating the value of node A, B, C and D. Similarly, green node B can receive information from red nodes 1, 2, 3 and 4. This is how two blocks communicate with each other. A bad interpolation is shown in Figure 25. The size of the outer boundary of the red grid is too small and the nearby wake grid is too big. There will be many red points inside one green element and linear interpolation can't guarantee each point receive true value of flow field information, especially when the flow changes dramatically in this element.

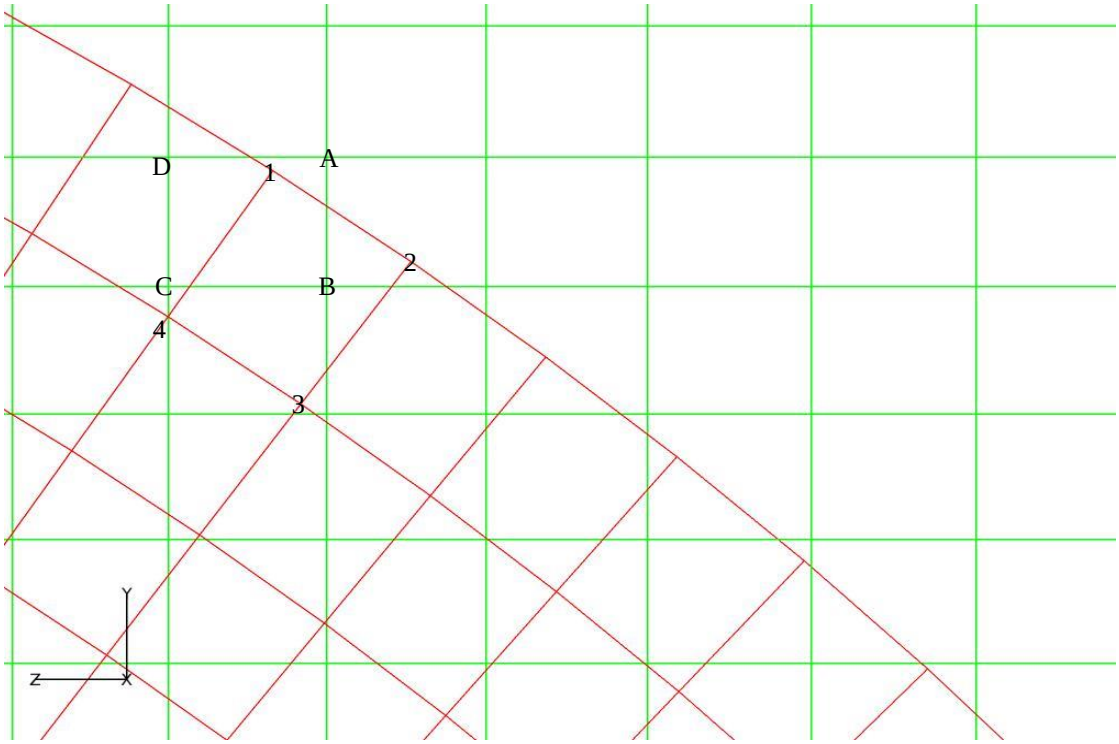

Figure 24 Interpolation Between Two Blocks

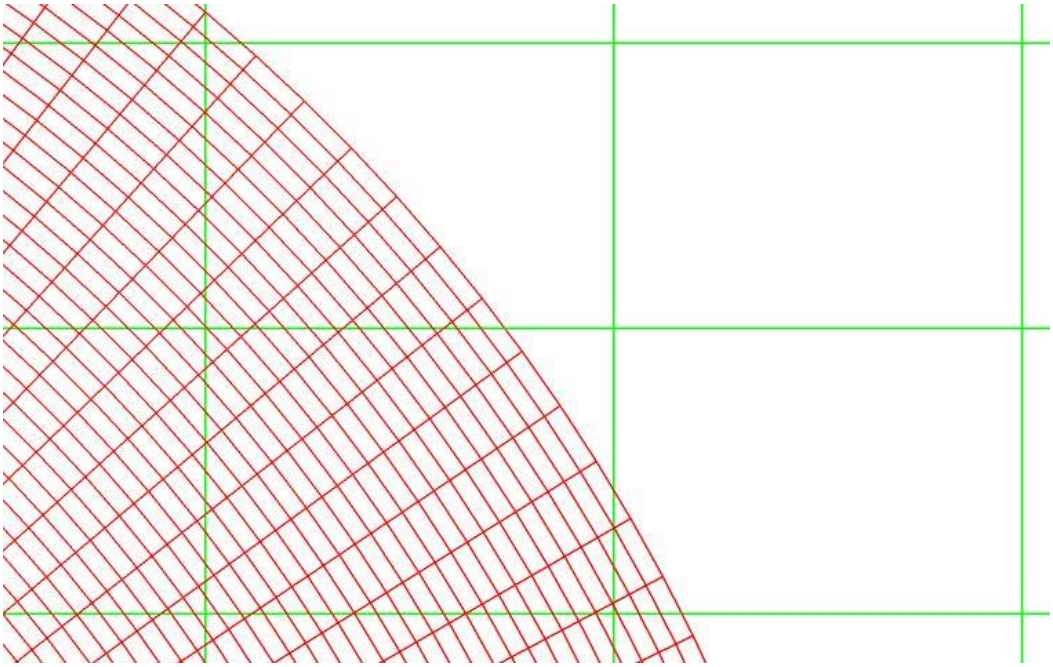

Figure 25 Bad Interpolation Between Two Blocks

The final step is to cut the hole inside the near wall. Grid points inside the near body grid are excluded. Figure 26 shows the remaining zigzag green gird which forms the inner boundary of the wake grid and will receive information from near body grid. Figure 27 shows the overlap between the remaining wake grid and the near body grid which ensure the interpolation between two blocks.

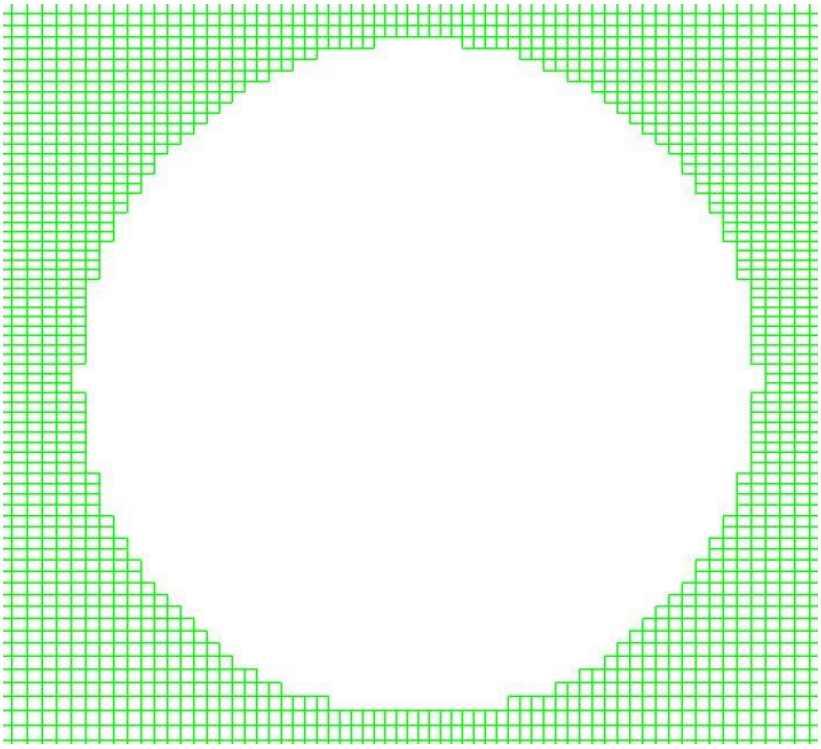

Figure 26 Wake Grid After Hole Cutting

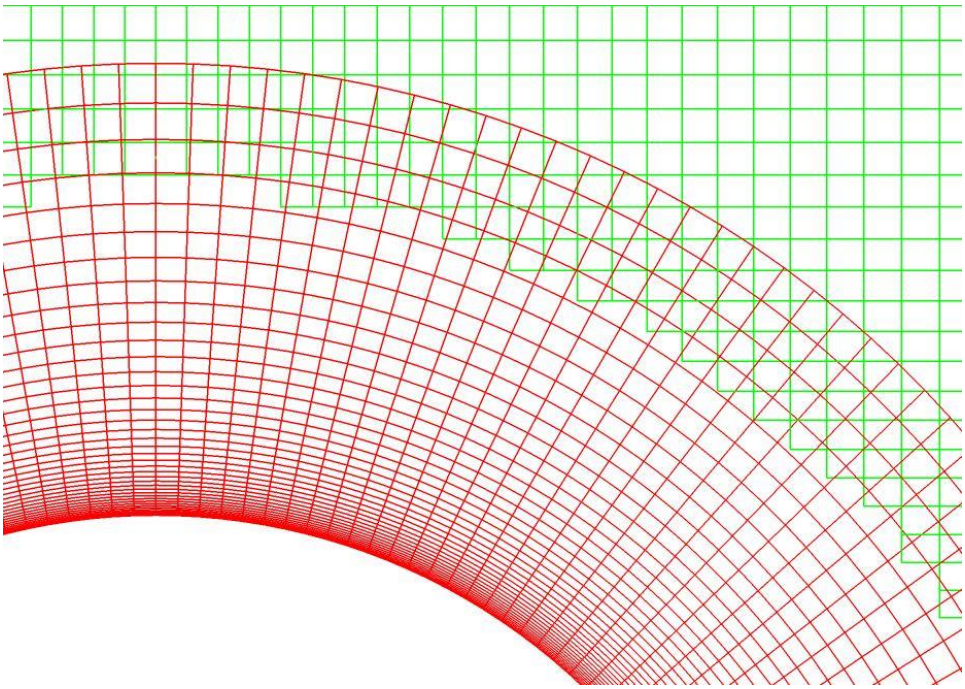

Figure 27 Hole Cutting of Overset Grid

Simulation Results

The simulation was performed under current speed 0.5 m/s and 0.83 m/s, as specified in the experimental tests. At the beginning, the riser was set straight, vertically standing in the still water. When the simulation starts, vortex starts to generate around the riser due to the current. Meanwhile, the top of the riser start to oscillate according to the prescribed motion. At the same time, the riser begins deflection in in-line direction.

A close look at the fixed end of the riser, shows the evolution of the vortex in the uniform current, as was shown in Figure 28.

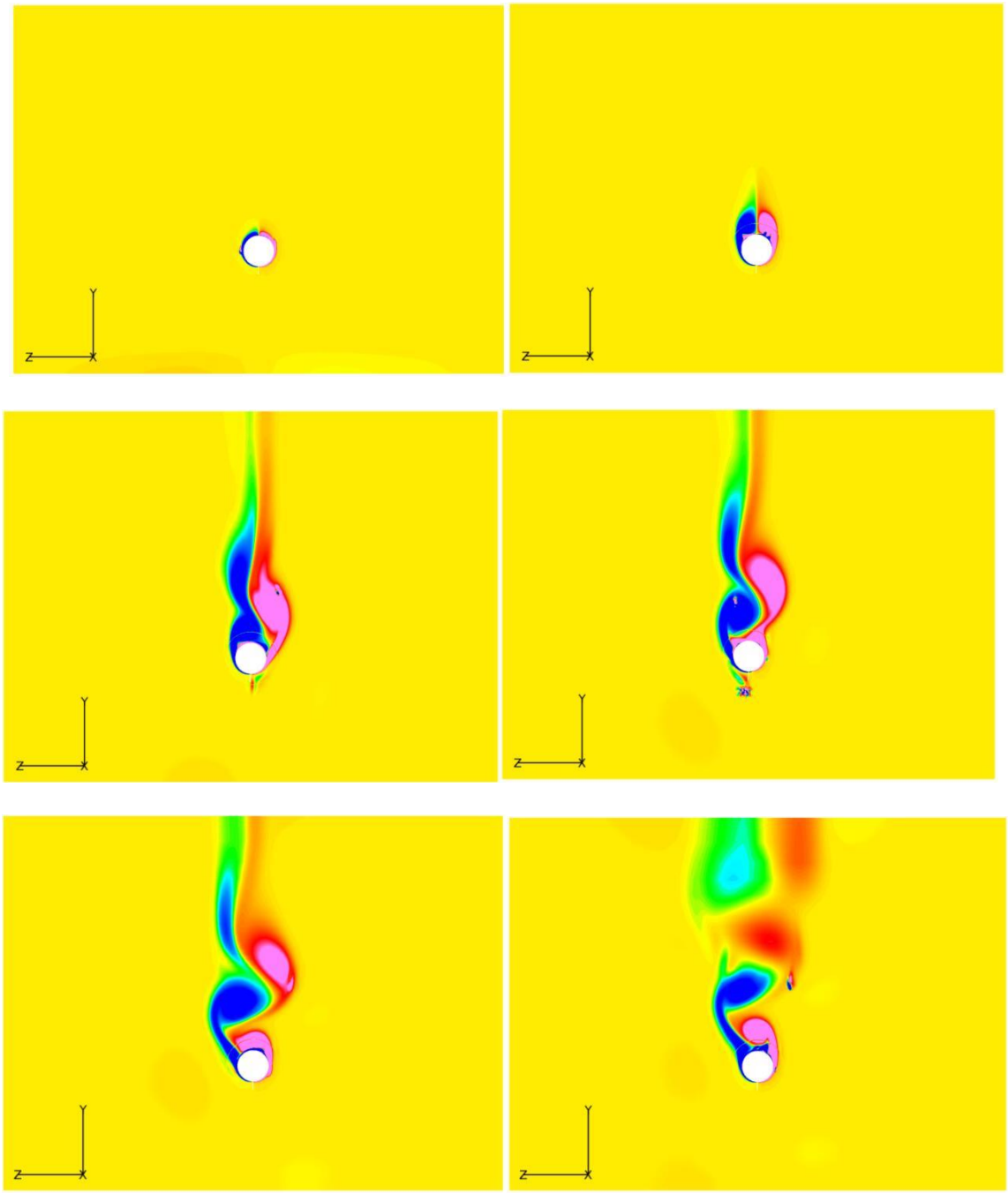

Figure 28 Vortex Evolution at Riser Bottom

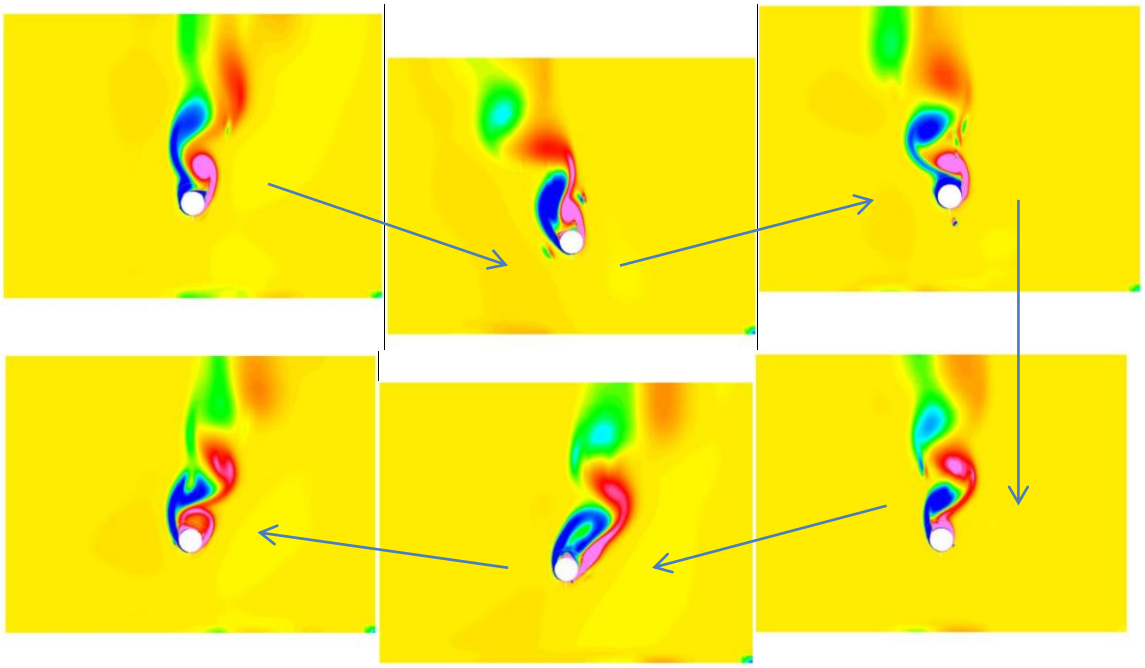

Figure 29 Motion at Riser Top

Figure 29 shows the motion at the top of the riser and the vortex generated. At both sides of the "banana shape", the riser velocity is zero and only uniform current coming in positive y direction. The vortex generated at these two ends sheds in y direction. The velocity reaches maximum at the middle of the "banana" shape. The vortex sheds in the direction of the relative velocity.

The deflection of the riser is presented in Figure 30. Under the current speed 0.5 m/s and 0.83 m/s, for both in-line and cross-flow, the deflection is small. The largest displacement occurs at the top of the riser. We can clearly observe the "banana shape" motion in y-z plane at the top of the riser. The envelope of the displacement is shown in

Figure 31. The results agree with the experimental data concluding that, at low current speed (0.5 m/s & 0.83 m/s), regular mode 1 is the dominant response.

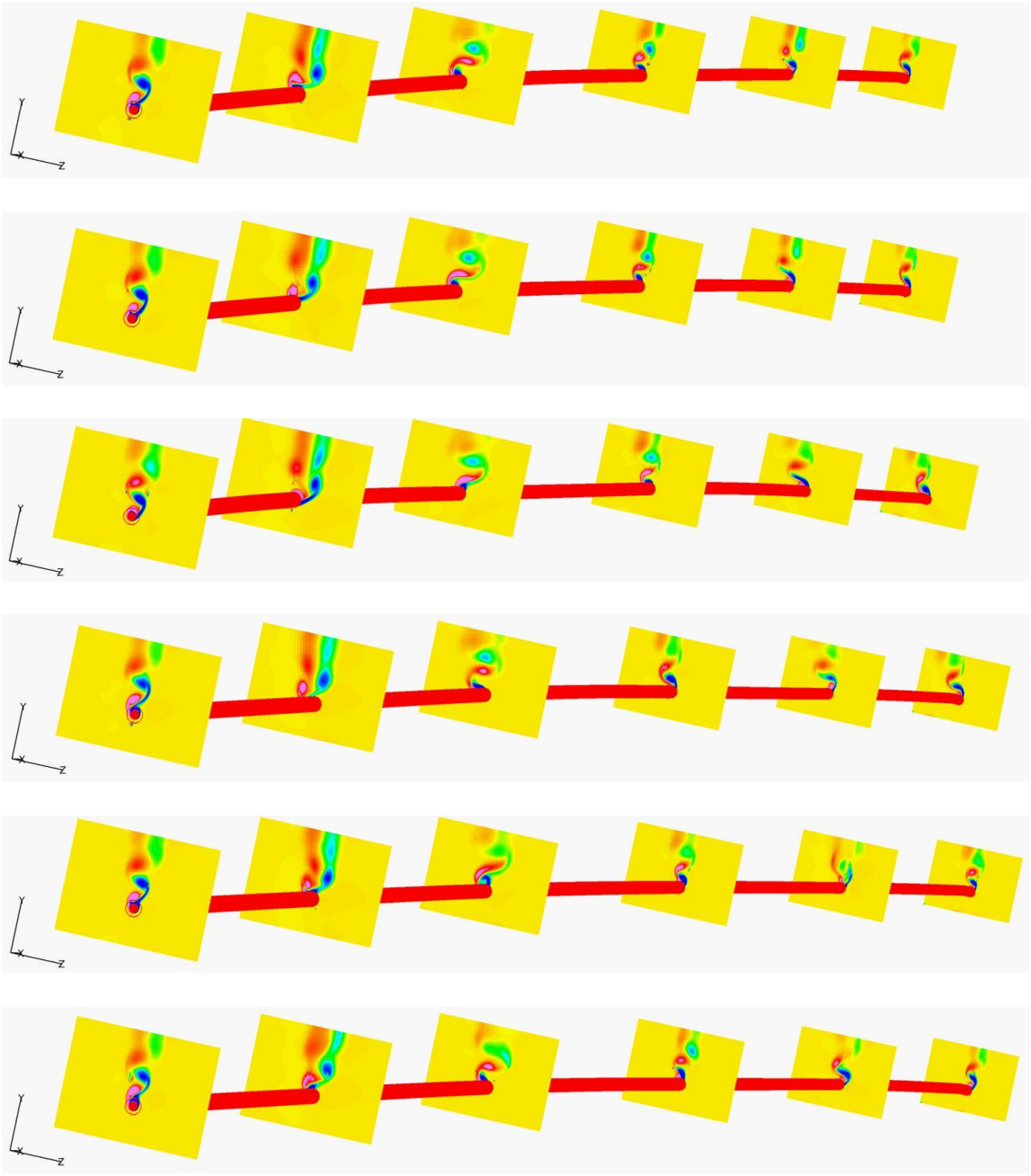

Figure 30 Riser Deflection

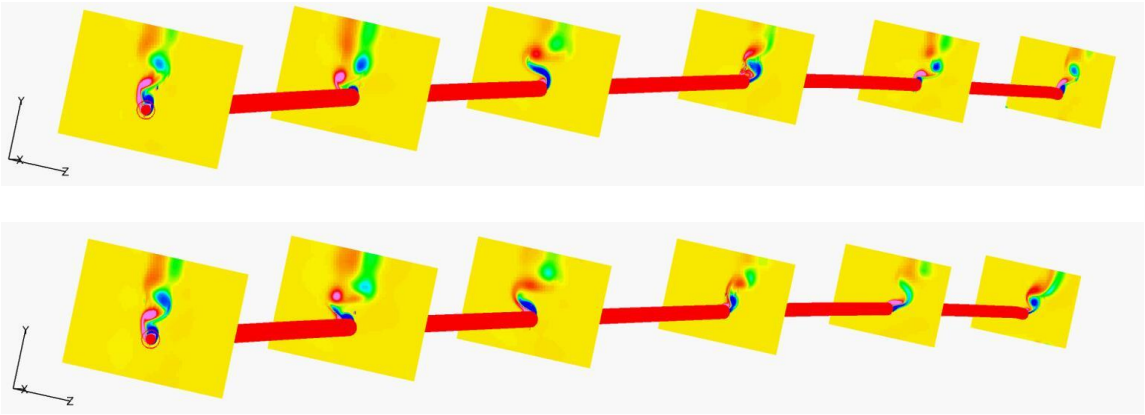

Figure 30 Continued

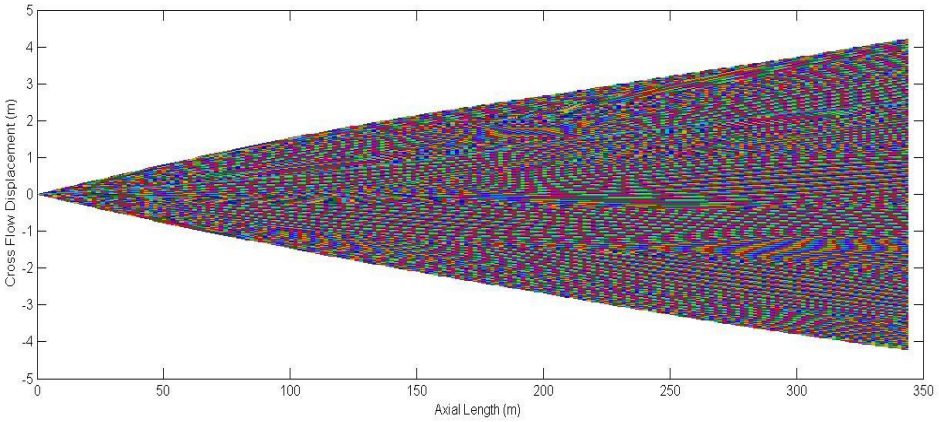

Figure 31 Displacement Envelope

The riser displacement history in the in-line and cross-flow directions at current speed 0.83 m/s is shown in Figure 32 and Figure 33 separately. The top sections are mostly subject to the prescribed motion. Thus, we choose the near bottom displacement as a representative. It should be notified that the prescribed motion is simulated in an equivalent stable status, which means the riser will oscillate near origin point (y = 0, z =

0) in both in-line and cross-flow direction. The time increment for each simulation step is 0.1 s.

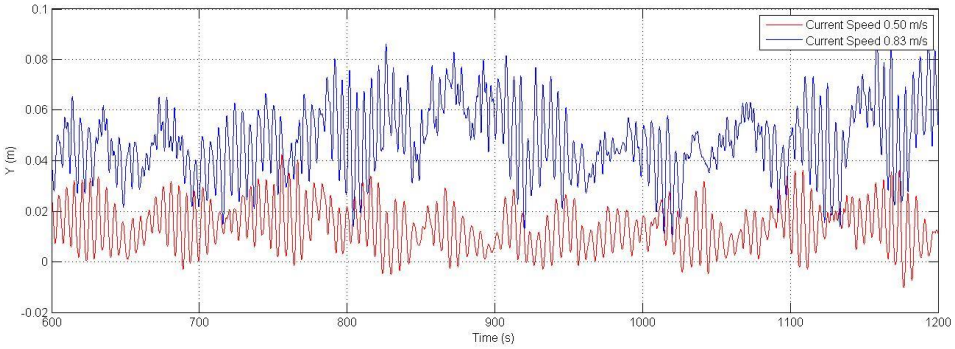

Figure 32 In-line Motion History

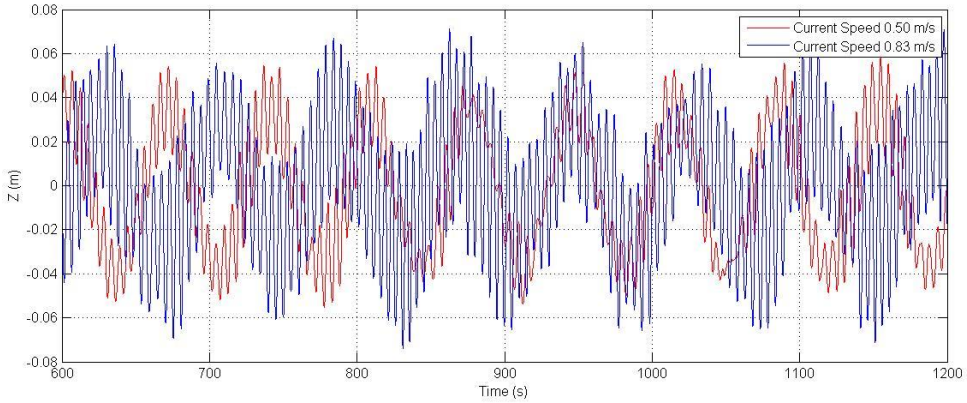

Figure 33 Cross Flow Motion History

Fast Fourier Transform was applied to study the frequency of the vibration in cross flow direction. To avoid the influence of the initiation, we use the data from time=500s to time=2000s. The result is presented in Figure 34. As we can observe, the first peaks for two current speeds occur near 0.02 Hz. This frequency is related to the

prescribed motion. The second peak occurs at 0.18 Hz for current speed 0.50 m/s and 0.2 Hz for current speed 0.83 m/s. This frequency is related to the vortex-induced vibration. Wilde's experiment gives the similar pattern for the cross flow loads at bottom of Riser, as shown in Figure 35. A possible explanation for the difference occurs at high frequency is that when prescribe the buoyancy can motion, we didn't include the high frequency components. While in the experiment, the buoyancy can actually has high frequency vibration.

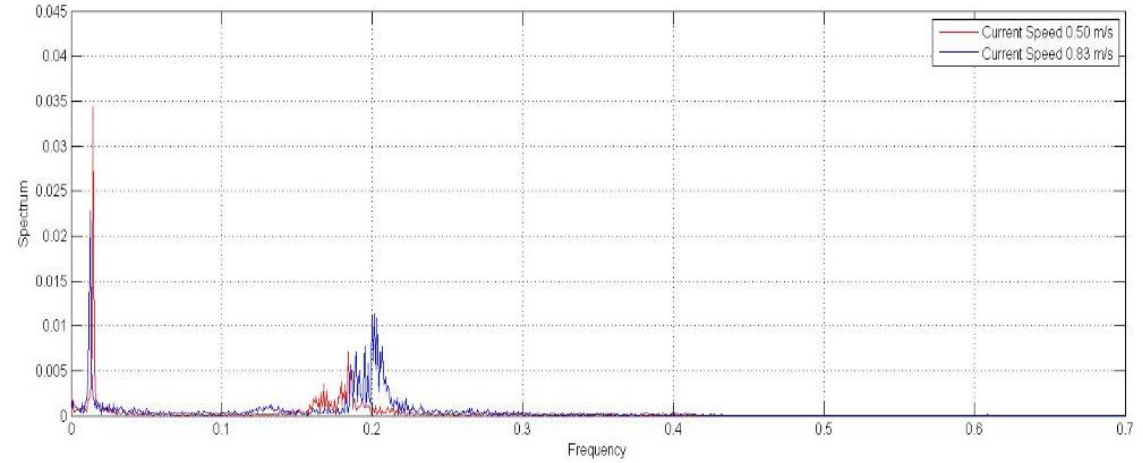

Figure 34 Spectrum of Motion at Bottom of Riser

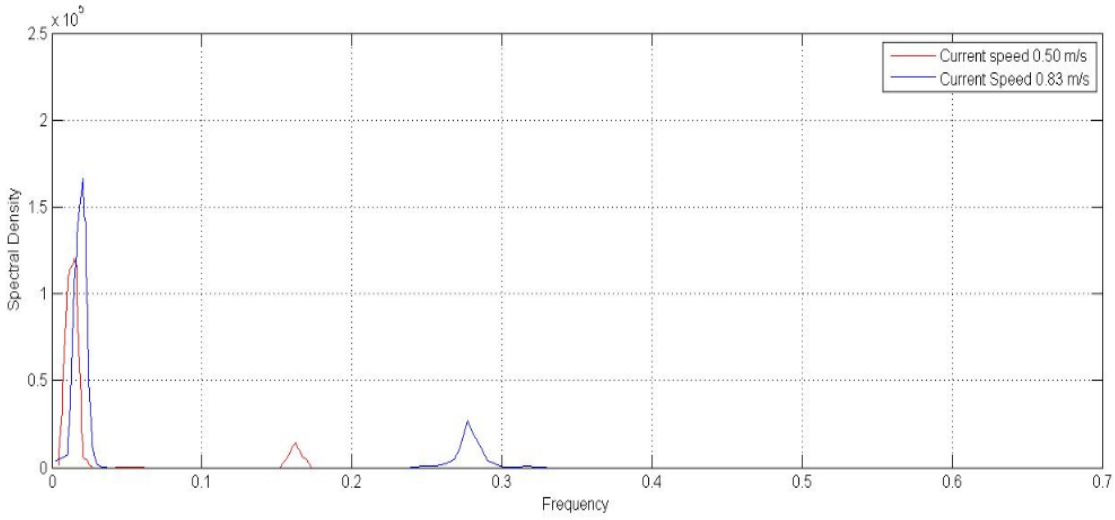

Figure 35 Spectrum of Cross Flow Loads at Bottom of Riser

The trajectory at bottom of the riser is presented in Figure 36 and Figure 37. This trajectory is quite different with what we usually observe in VIV research. It is not in "figure eight" or "banana shape". In fact, it is a combination of two shapes. First the riser follows the prescribed motion which is a large "banana shape". Then, due to the VIV, the riser also has a "figure eight" motion with much smaller amplitude. Thus, we can see an overall "banana shape" consisting of many small irregular "figure eight".

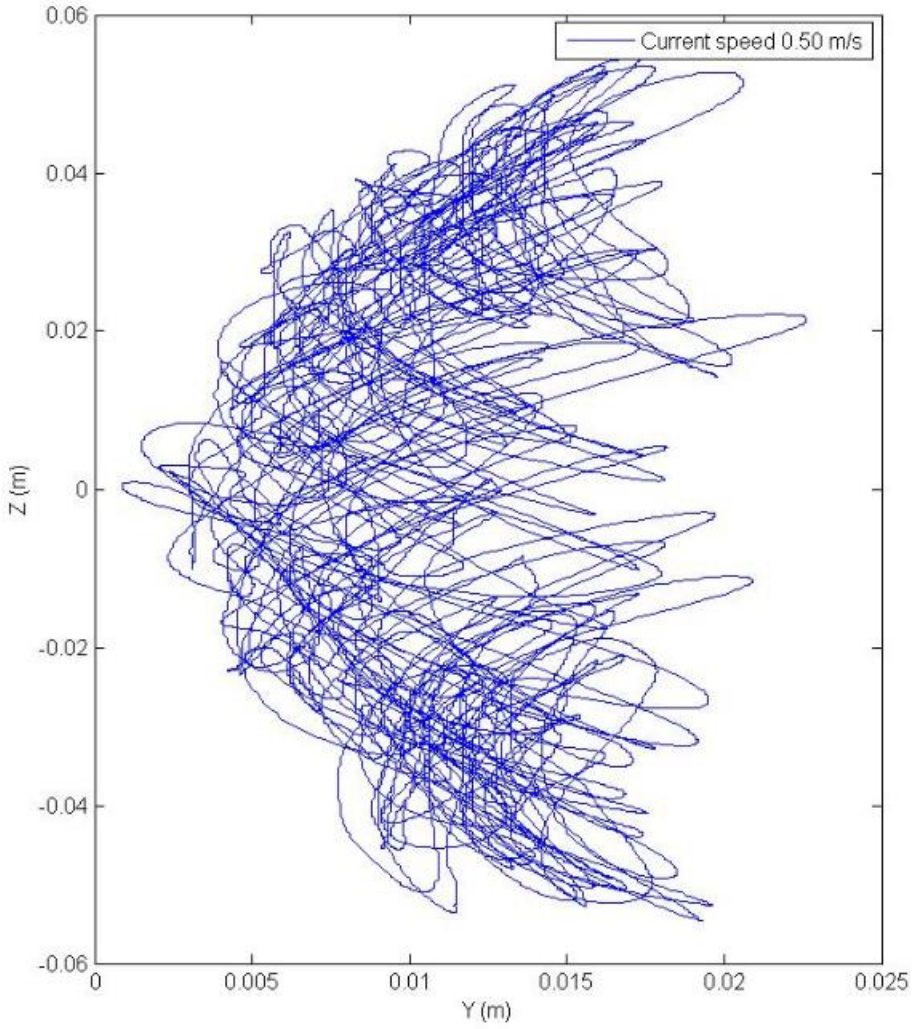

Figure 36 Trajectory at bottom for current speed 0.50 m/s

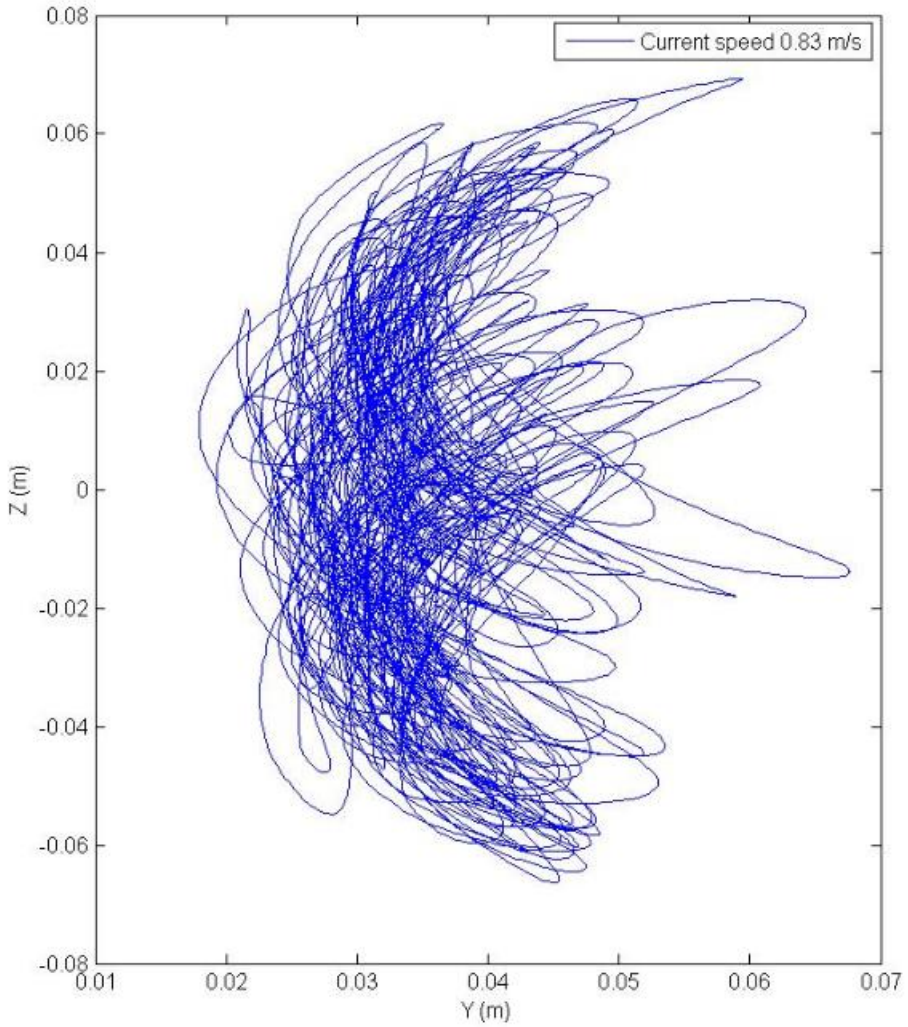

Figure 37 Trajectory at bottom for current speed 0.83 m/s

If we plot the trajectory with only a few time steps, we can observe the small "figure eight" more clearly. For example, Figure 38 shows the trajectory for current speed 0.83 m/s during time =100 s to time =110 s. The riser is doing "figure eight" motion with z roughly ranging from -0.06 m to 0.01 m. Figure 39 shows the following 10 seconds of the trajectory. And Figure 40 shows the next 10 seconds of the trajectory. The trajectories are following "banana shape" or "figure eight" and the mean position of

the oscillation is moving upward in z direction. This phenomenon helps illustrate that the trajectories shown in Figure 36 and Figure 37 are consisting of one prescribed “banana shape” and the small “figure eight” caused by VIV.

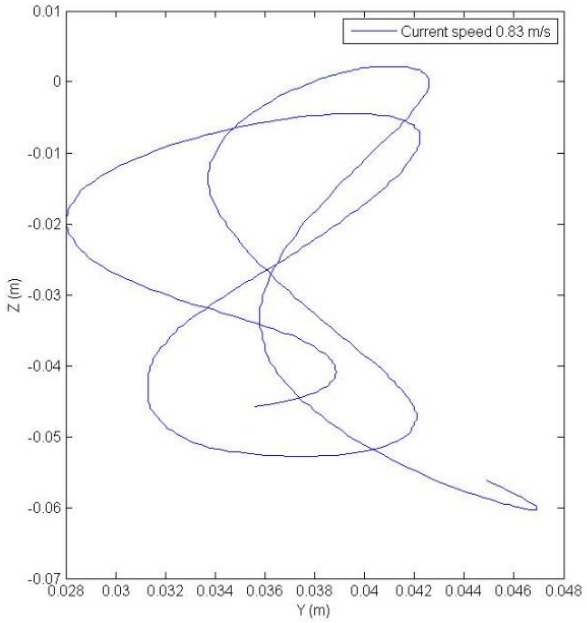

Figure 38 Trajectory for Current Speed 0.83 m/s During Time =100 s to Time =110 s

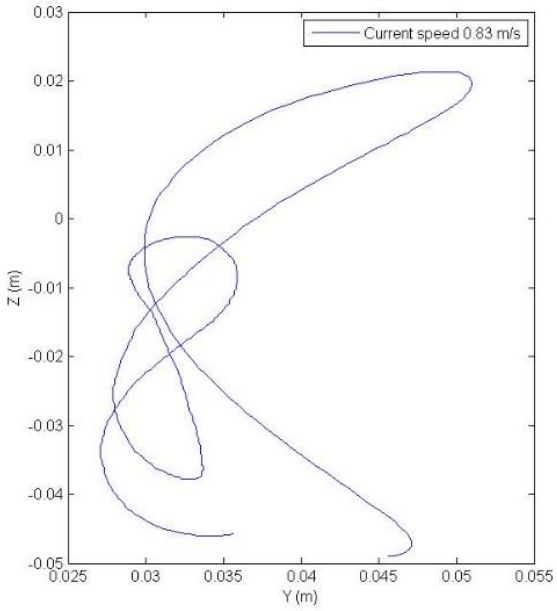

Figure 39 Trajectory for Current Speed 0.83 m/s during Time =110 s to Time =120 s

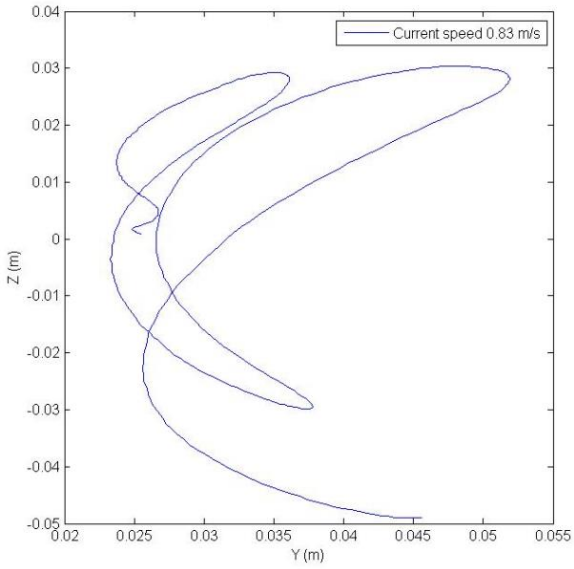

Figure 40 Trajectory for Current Speed 0.83 m/s during Time =120 s to Time =130 s

Figure 41 – Figure 43 show the trajectories at 0.2 L, 0.4 L, 0.6 L and 0.8 L of the Riser. As the location approaches to the top, the prescribed motion become increasingly dominant and the influence of vortex-induced vibration become decreasingly effective. These figures also help illustrate that the trajectories are combined with two shapes of motion.

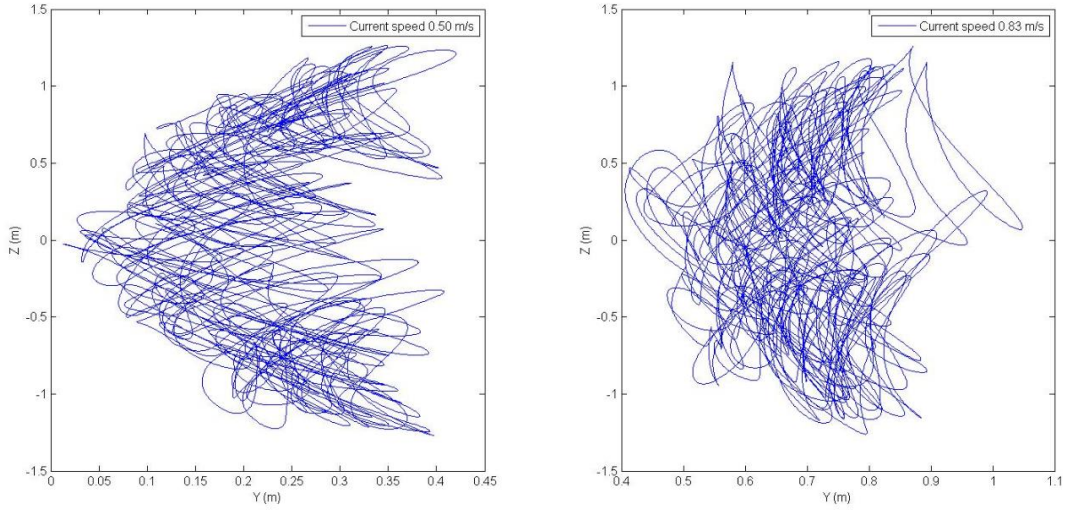

Figure 41 Trajectories at 0.2 L of Riser

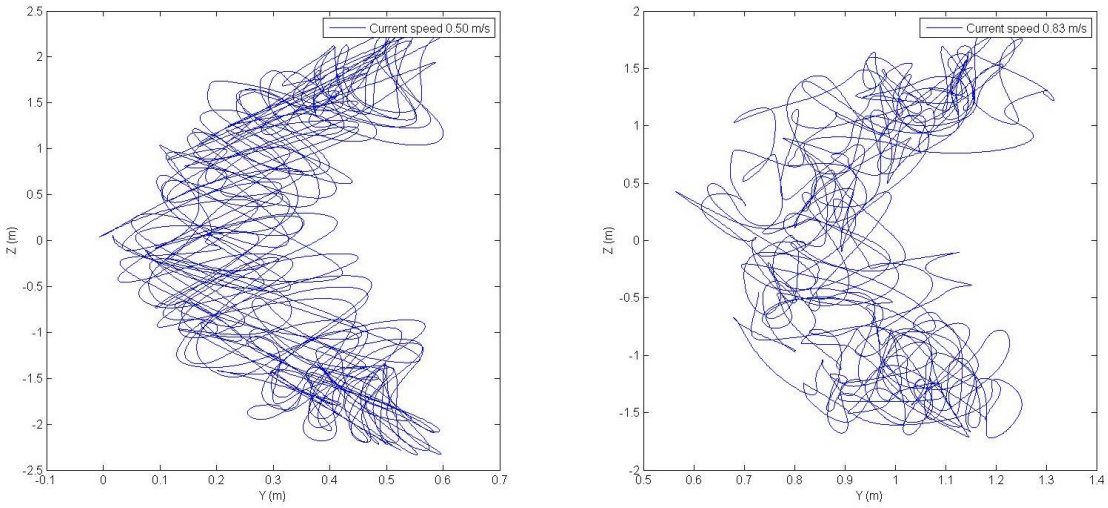

Figure 42 Trajectories at 0.4 L of Riser

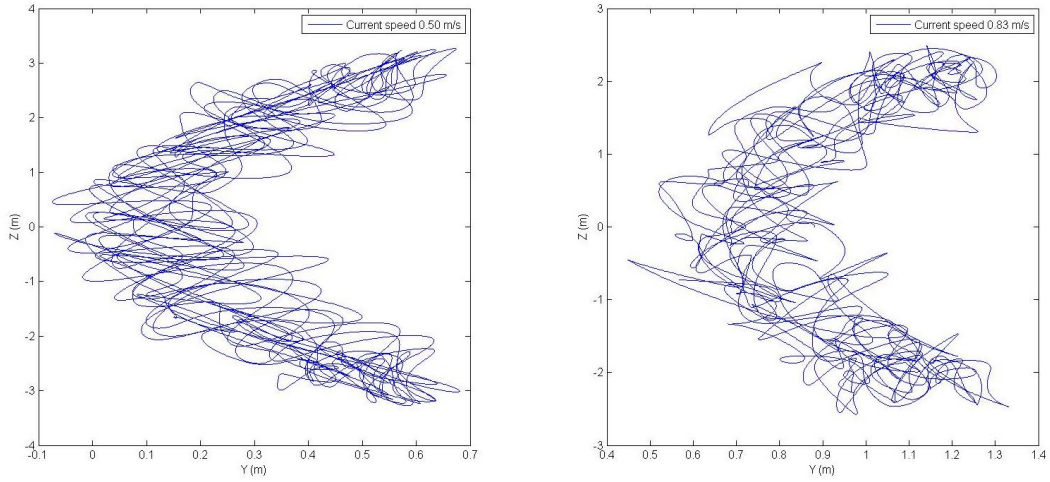

Figure 43 Trajectories at 0.6 L of Riser

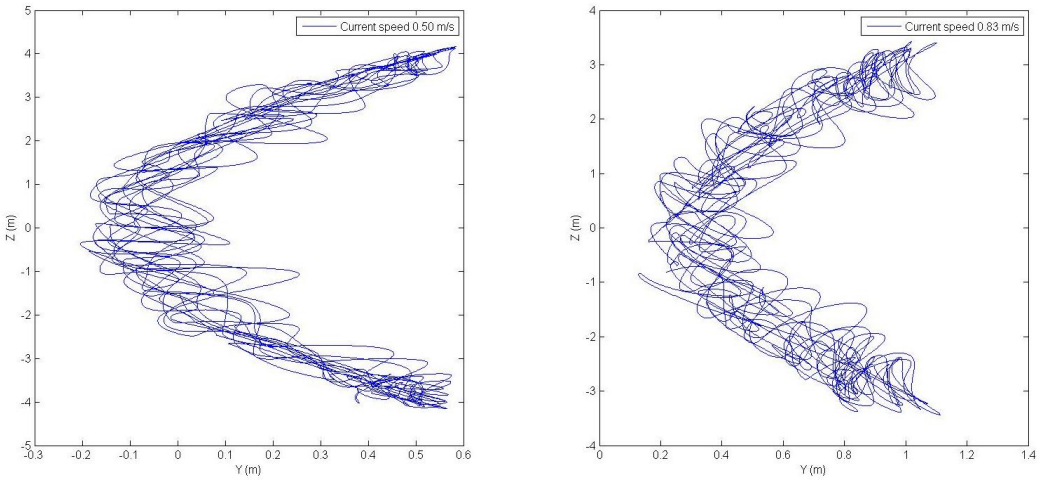

Figure 44 Trajectories at 0.8 L of Riser

CHAPTER IV

VIV SIMULATION OF A RISER UNDER REGULAR WAVE

In many previous riser VIV simulations, the riser was assumed to be fixed on two sides. However, in reality, it is not always the case. Attached to the platform, the top of the Riser will move with the platform. In the next part of the thesis, we are going to study a riser which is connected to the platform. The coupled system is under harmonic regular wave. No current is applied. We simplify the case by prescribing a sinusoid motion at the top of the riser to replace the platform motion. Wilde's FSHR parameters were used as reference. For a 300 m depth TLP vibration, the amplitude is about 5 m and the frequency is below 1 Hz (Adrezin et al., 1999). The sinusoid motion is prescribed in z direction, with an amplitude of 5 m, and a frequency of 0.083 rad/s.

Grid Generation

Before CFD calculation, a new grid needs to be generated for this special case. Since there is no current coming in y direction, vortex shedding in y direction won't be as remarkable as before. Thus, in order to improve computational efficiency, we can narrow the dimension in y direction and move the riser to the center of the grid.

The new grid is shown in Figure 45. The riser was put in the center of the grid. The grid is 16 D (Diameter of the Riser) in y direction and 40 D in z direction. Red block consists of 373100 (50*182*41) grid points and green block consists of 854550 (50*81*211) grid points. There are about 1.2 million computational nodes in this simulation.

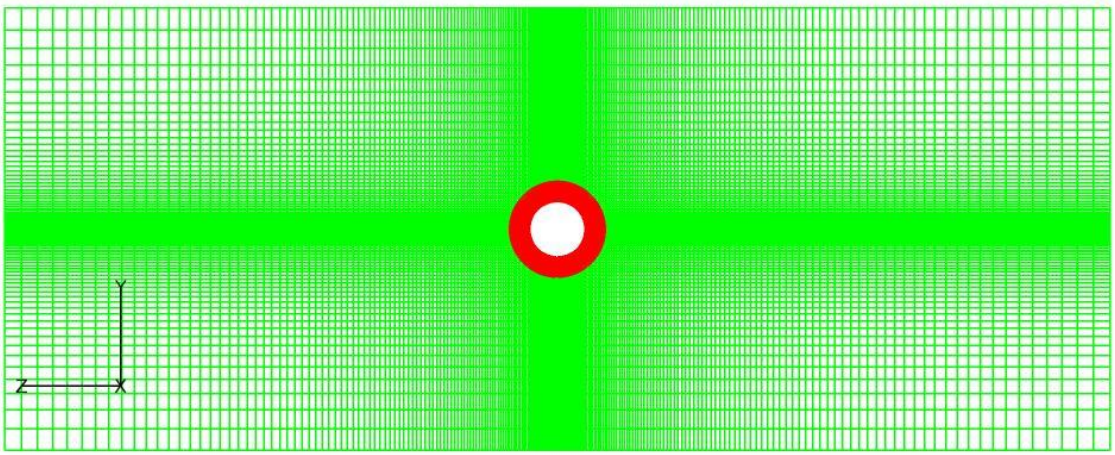

Figure 45 Overset Grid for VIV Simulation of Riser under Regular Wave

A close view of the near wall grid is presented in Figure 46. For the near body grid, we set the size as 0.001 D. As it departs from the wall, the grid size gradually increases to 0.025 D at the intersection with the wake grid. For green block, the grid size is 0.025 D in the middle and 0.4 D at the far way area in y direction. As for z direction, the grid size ranges from 0.025 D to 0.3 D. The interpolation between two blocks is guaranteed.

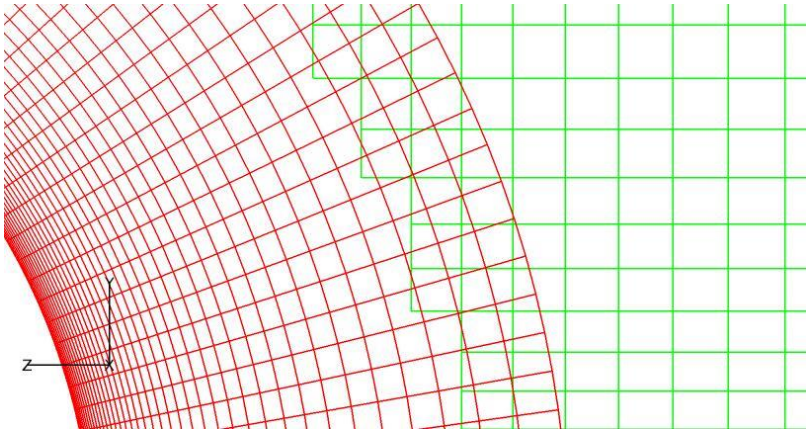

Figure 46 Interpolation between Two Blocks

Simulation Results

Figure 47 shows the motion on the top of the Riser. Due to the sinusoid motion prescribed, vortex sheds behind the Riser. It can be observed clearly, that vortex shedding is related to the speed of the oscillation. The relative speed reaches a maximum when the riser is passing the center of the harmonic vibration and the vortex leaves the riser very quickly. After that point, the riser start to decelerate, and the speed of vortex shedding also slows down. When the riser finally stops, vortex shedding also stops. Then the riser starts to move back, breaking the vortex generated before, creating new vortex.

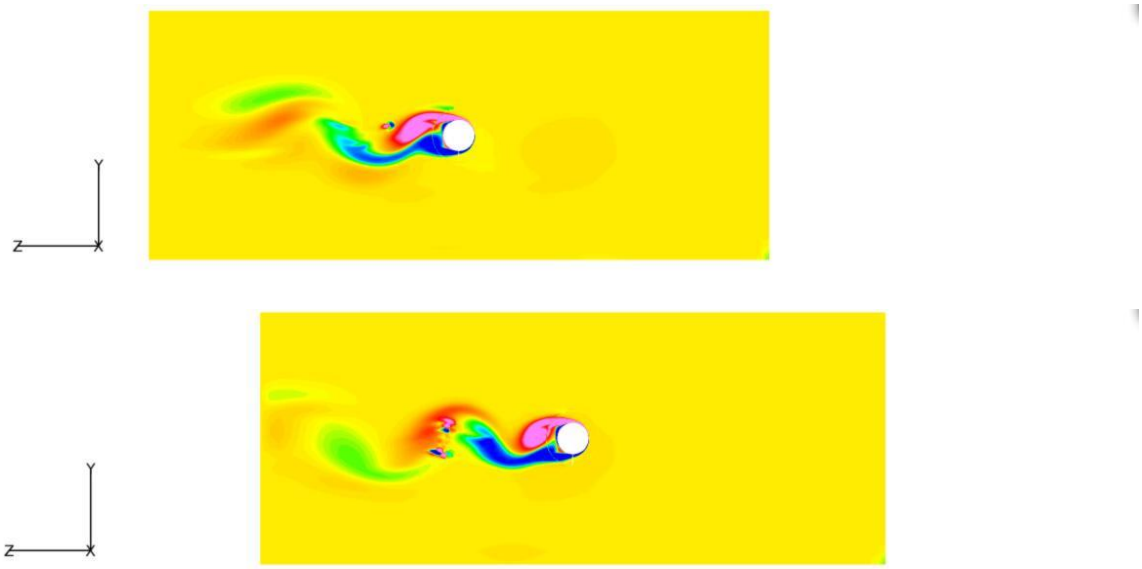

Figure 47 Vortex Shedding at top of the Riser

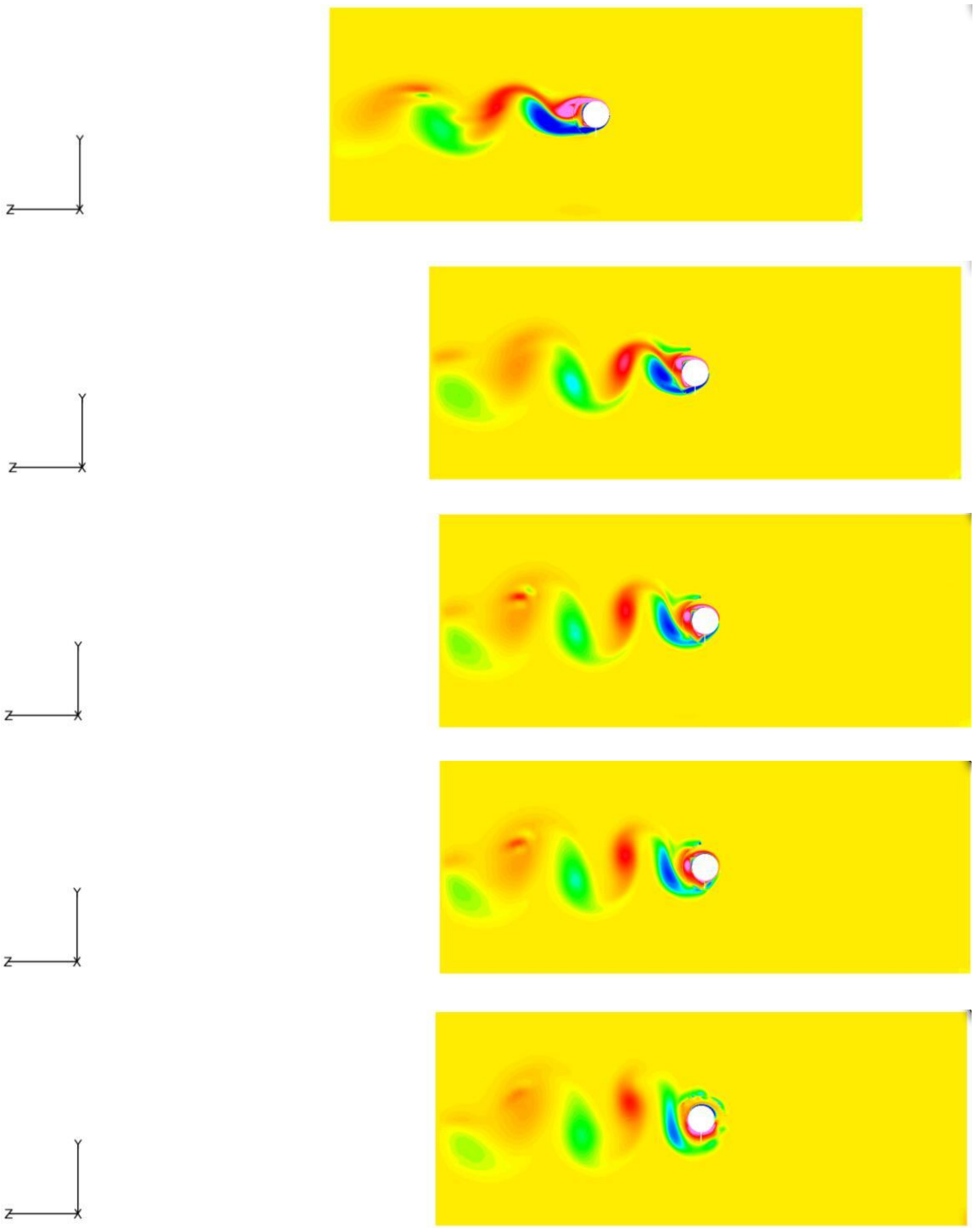

Figure 47 Continued

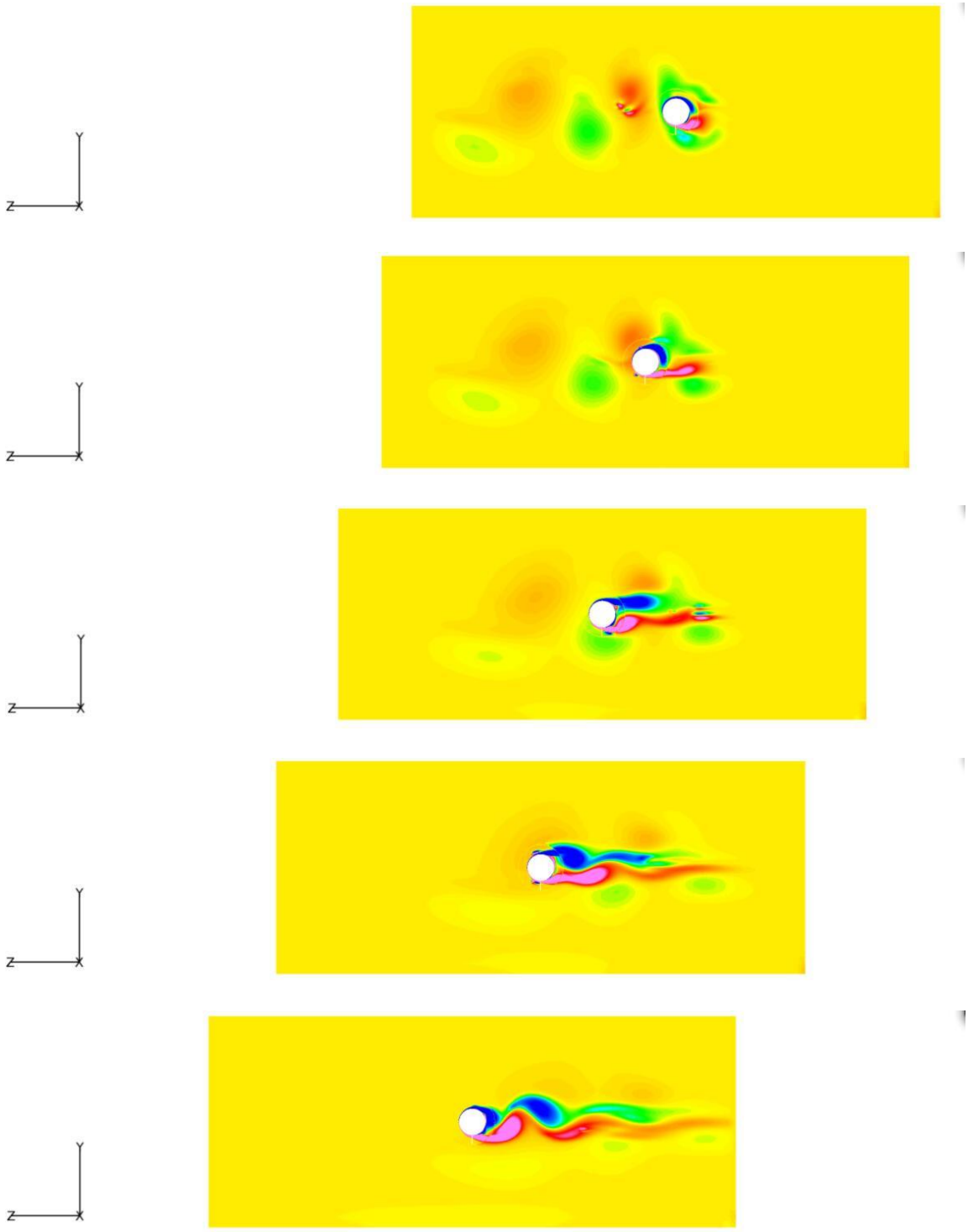

Figure 47 Continued

Figure 48 shows the Vibration History in z direction at lower section of the riser (0.4 L). The reason we choose that location to study is because at the top of riser, the motion is subject to the prescribed motion, while at the bottom, the motion is too small to create vortex. As is shown in the plots, there is no vortex induced vibration can be visually observed in z direction. The motion in z direction mostly follows the prescribed vibration. However, we can write z motion in equation (24). After subtracting the mean motion, we can clearly observe the VIV fluctuation in Figure 49.

$$Z = \bar{Z} + Z' \tag{24}$$

Where $\bar{Z} = \bar{A}\sin(\bar{w} * t)$ is the mean motion in z direction and Z' is the fluctuation of the motion.

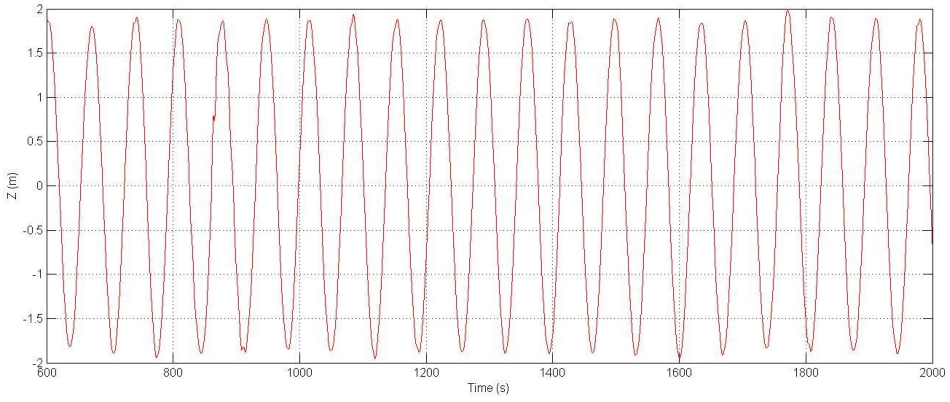

Figure 48 Motion History in Z Direction

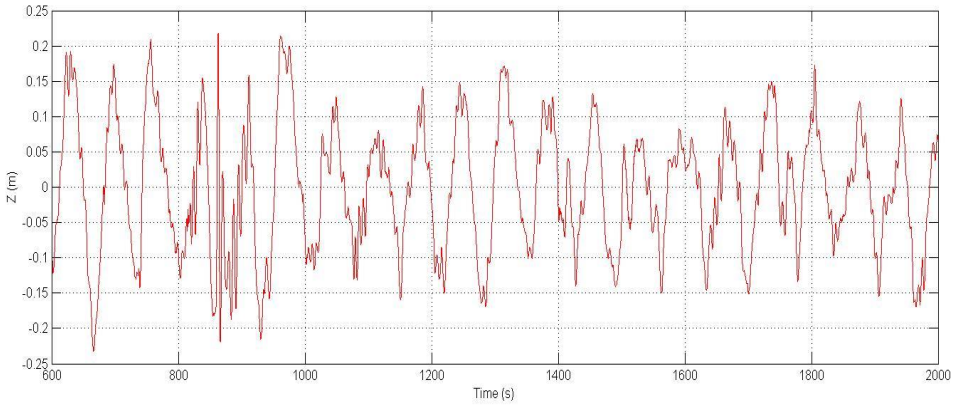

Figure 49 Small-Amplitude VIV in Z Direction

While in y direction, as presented in Figure 50, due to lack of prescribed motion, VIV can be observed easily. The motion mostly ranges from – 0.1 m to 0.1 m. No distinguishable frequency is observed in this case.

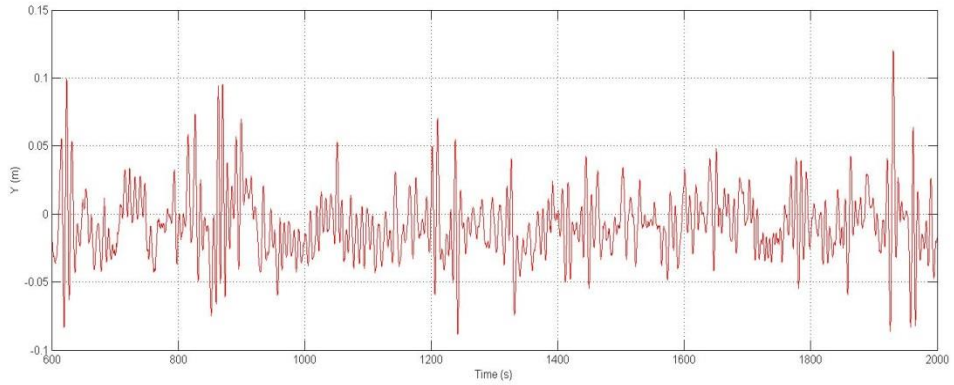

Figure 50 Motion History in Y Direction

The results were analyzed using a FFT (Fast Fourier Transform) to study the motion in y direction. As shown in Figure 51, Most of the peaks occur from 0 Hz to 0.15 Hz. There is a rough “V” shape for the spectrum in the range from 0 Hz to 0.15 Hz. Still

there is no main frequency can be found. A possible explanation is that due to the sinusoid oscillation, there will be no steady relative velocity between riser and the fluid. It is like constantly varying current passing the riser, the VIV is expected to be irregular.

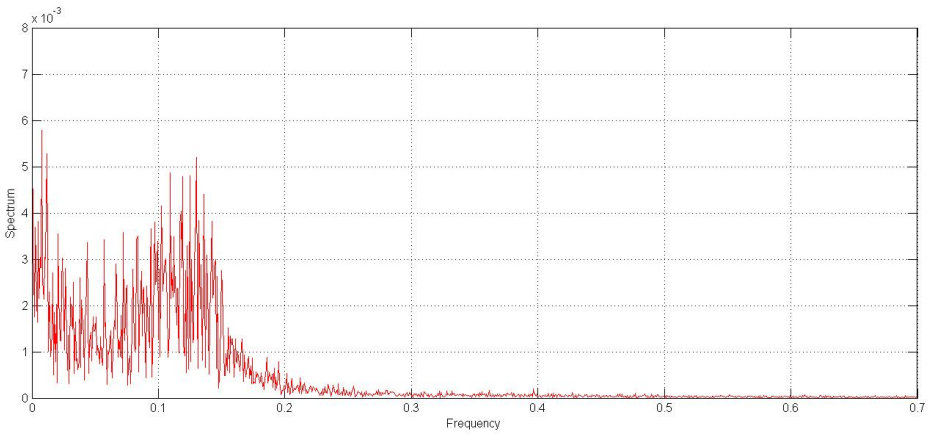

Figure 51 Frequency in Y Direction

The trajectory of the motion is presented in Figure 52. The riser is mainly following the prescribed motion in z direction. Vortex induced vibration in y direction is relatively small compared to the motion in z direction. At right and left ends of the oscillation, due to the prescribed motion velocity decreasing to zero, riser stays longer at these locations. Thus, there are more vibrations in y direction at two ends. Also due to the relative small velocity between riser and flow at these areas, the amplitude of the VIV is relatively small. Riser is moving backward and breaking the vortex generated before. Thus the vibration tends to be more chaotic at these locations.

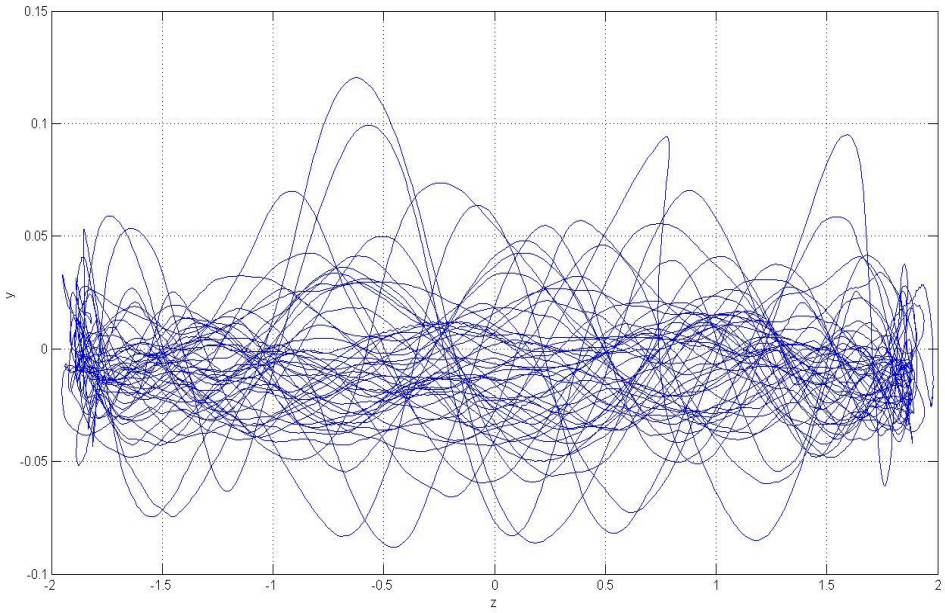

Figure 52 Trajectory of the Riser

CHAPTER V

SUMMARY AND CONCLUSIONS

Vortex-induced vibrations of vertical risers have been investigated in many previous experimental studies, but so far, only a few tests have been done for Free Standing Hybrid Riser VIV. Numerical simulations, using Finite-Analytic Navier-Stokes (FANS) code, have been tested with many vertical risers cases. However, simulation with a prescribed motion at top side of the riser hasn't been fully studied yet. In this thesis, we first developed a riser motion solver by discretizing tensioned beam governing equations. Then we coupled the motion solver with a three-dimensional CFD solver to achieve Fluid-Structure Interactions. Overset grid and dynamic grid techniques are adopted in the CFD approach to facilitate time-domain simulation of the riser motion without tedious and time-consuming grid regeneration.

At the beginning of the research, a static test was conducted to validate the motion solver. The results show perfect agreement with the analytic solutions. Then a dynamic test with one side pinned and one side with an applied a sinusoid motion was conducted. The results generally agree with the simulation by OrcaFlex.

First case of the simulation is based on Wilde's model test on the VIV of the air can of a FSHR. The simulation simplifies the case by using prescribed motion to replace the motion of the air can. All the input riser parameters are based on the experiment including diameters, length, Young's modulus, weight per length, tension, etc. The in-line and cross-flow motion history, VIV amplitude and frequency, and riser trajectory

have been investigated. The results indicate that the riser is subject to both the prescribed motion and the vortex-induced vibration. Thus the trajectory of the riser is different with the common “figure eight” or “banana shape”. It is a combination of the prescribed “banana shape” and the vortex-induced “figure eight”.

Second case is to simulate a riser connected with a platform, while the platform is under a harmonic regular wave. No current is applied. Still, we simplify the case by prescribing a sinusoid motion in z direction to replace the movement of the platform. The riser input parameters we use are the same as the one in Wilde’s experiment. Vortex is generated behind the riser as it moves. The faster riser moves, the faster vortex sheds. VIV can be found in both y and z directions. Complex vibration appears at two ends, where the riser moves backwards and breaks the previous vortex.

In conclusion, a fully three-dimensional CFD approach for VIV simulation for a top side moving Riser has been presented. The riser VIV response is computed in according to the unsteady, incompressible Navier-Stokes equations in conjunction with a large eddy simulation model. More experiments need to be conducted to do the comparison. The numerical simulation results shed some light on the FSHR VIV problems.

REFERENCES

Adrezin, R., and H. Benaroya. "Non-linear stochastic dynamics of tension leg platforms." Journal of Sound and Vibration 220.1 (1999): 27-65.

Chen, H. C., C. R. Chen, and K. Huang. "CFD simulation of vortex-induced and wake-induced vibrations of dual vertical risers." The Twenty-third International Offshore and Polar Engineering Conference. International Society of Offshore and Polar Engineers, 2013.

Chen, H. C., and V. C. Patel. "Near-wall turbulence models for complex flows including separation." AIAA Journal 26.6 (1988): 641-648.

Chen, H. C., and V. C. Patel. "The flow around wing-body junctions." Symposium on Numerical and Physical Aspects of Aerodynamic Flows, 4 th, Long Beach, CA. 1989.

Chen, H. C., V. C. Patel, and S. Ju. "Solutions of Reynolds-averaged Navier-Stokes equations for three-dimensional incompressible flows." Journal of Computational Physics 88.2 (1990): 305-336.

Cheng, Y. M., and K. F. Lambrakos. "Time domain computation of riser VIV from vessel motions." 25th International Conference on Offshore Mechanics and Arctic Engineering. American Society of Mechanical Engineers, 2006.

Cheng, Y. M., and K. F. Lambrakos. "Time domain riser VIV predictions compared to field and laboratory test data." ASME 2007 26th International Conference on Offshore Mechanics and Arctic Engineering. American Society of Mechanical Engineers, 2007.

Huang, K., H. C. Chen, and C. R. Chen. "Riser VIV analysis by a CFD approach." The Seventeenth International Offshore and Polar Engineering Conference. International Society of Offshore and Polar Engineers, 2007.

Huang, K., H. C. Chen, and C. R. Chen. "Riser VIV induced fatigue assessment by a CFD approach." The Eighteenth International Offshore and Polar Engineering Conference. International Society of Offshore and Polar Engineers, 2008.

Huang, K., H. C. Chen, and C. R. Chen. "Numerical scheme for riser motion calculation during 3-D VIV simulation." Journal of Fluids and Structures 27.7 (2011): 947-961.

Huang, K., H. C. Chen, and C. R. Chen. "Vertical riser VIV simulation in sheared current." International Journal of Offshore and Polar Engineering 22.02 (2012).

Liu, N., Y. Cheng, J. D. Wilde, R. Burke, and K. F. Lambrakos. "Time domain VIV Analysis of a free standing hybrid riser." ASME 2009 28th International Conference on Ocean, Offshore and Arctic Engineering. American Society of Mechanical Engineers, 2009.

Pereira, P. S. D., K. Maeda, C. K. Morooka, K. Tamura, and K. Itoh. "Experimental study on a self standing hybrid riser system throughout tests on a deep-sea model basin." ASME 2005 24th International Conference on Offshore Mechanics and Arctic Engineering. American Society of Mechanical Engineers, 2005.

Pontaza, J. P., C. R. Chen, and H. C. Chen. "Chimera Reynolds-averaged Navier-Stokes simulations of vortex-induced vibration of circular cylinders." Civil Engineering in the Oceans VI. 2006. 166-176.

Pontaza, J. P., C. R. Chen, and H. C. Chen. "Simulation of High Reynolds Number Flow past Arrays of Circular Cylinders Undergoing Vortex-induced Vibrations." The Fifteenth International Offshore and Polar Engineering Conference. International Society of Offshore and Polar Engineers, 2005.

Rakshit, T., S. Atluri, and C. Dalton. "VIV of a composite riser at moderate Reynolds number using CFD." Journal of Offshore Mechanics and Arctic Engineering 130.1 (2008): 011009.

Rehman, M.U., C. Vuik, and G. Segal. Preconditioners for the incompressible Navier-Stokes equations. Delft University of Technology, 2007.

Song, R. X., P. Stanton, and X. L. Zhou. "Engineering design of deepwater free standing hybrid riser." ASME 2010 29th International Conference on Ocean, Offshore and Arctic Engineering. American Society of Mechanical Engineers, 2010.

Wang, J. S., H. Liu, S. Q. Jiang, L. B. Xu, and P. L. Zhao. "Vortex-induced vibration on 2D circular riser using a high resolution numerical scheme." Journal of Hydrodynamics, Ser. B 22.5 (2010): 954-959.

Wilde J. Model tests on the vortex induced motions of the air can of a free standing riser system in current[C]//Proc. of DOT Conference. 2007.

Xiao, F. CFD Simulation of Vortex–Induced Vibrations of Free Span Pipelines Including Pipe-Soil Interactions. Diss. Texas A&M University, 2015.